ESAIM: M2AN
https://doi.org/10.1051/m2an/2023030

ESAIM: Mathematical Modelling and Numerical Analysis
www.esaim-m2an.org

A NEW TWO-DIMENSIONAL BLOOD FLOW MODEL WITH ARBITRARY CROSS SECTIONS

Cesar Alberto Rosales-Alcantar* and Gerardo Hernández-Dueñas

Abstract. A new two-dimensional model for blood flows in arteries with arbitrary cross sections is derived. The domain consists of a narrow, large vessel that extends along an axial direction, with cross sections described by radial and angular coordinates. The model consists of a system of balance laws for conservation of mass and balance of momentum in the axial and angular directions. The equations are derived by applying asymptotic analysis to the incompressible Navier-Stokes equations in a moving domain with an elastic membrane, and integrating in the radial direction in each cross section. The resulting model is a system of hyperbolic balance laws with source terms. The main properties of the system are discussed and a positivity-preserving well-balanced central-upwind scheme is presented. The merits of the scheme will be tested in a variety of scenarios. In particular, simulations using an idealized aorta model are shown. We analyze the time evolution of the blood flow under different initial conditions such as perturbations to steady states, which parametrizes a bulging in a vessel's wall. We consider different situations given by distinct variations in the vessel's elasticity.

Mathematics Subject Classification. 35L65, 65M06, 92Cxx.

Received October 17, 2022. Accepted March 28, 2023.

1. Introduction

The impact of cardiovascular diseases in our lives has motivated the development of different models for blood flows. In [11], a review of recent contributions towards the modeling of vascular flows is provided. A review of contributions regarding the mathematical modeling of the cardiovascular system is presented in [34]. In particular, the challenges in the mathematical modeling both for the arterial circulation and the hearth function are discussed. See also the notes in [32] for more on mathematical modeling and numerical simulation of the cardiovascular system. In [2], an open-source software framework for cardiovascular integrated modeling and simulation (CRIMSON) is described, which is a tool to perform three-dimensional and reduced-order computational haemodynamics studies for real world problems.

Three-dimensional (3D) models provide very detailed information of the fluid's evolution. In [22], fluid velocities were measured by laser Doppler velocimetry under conditions of pulsatile flow and such measurements were compared to those given by steady flow conditions. In [37], anatomic and physiologic models are obtained with the aid of 3D imaging techniques for patient-specific modeling. For instance, 3D hemodynamics in compliant

Keywords and phrases. Blood flow models, Hyperbolic conservation laws, Central-upwind schemes, Well-balance, Positivity-preserving schemes.

Institute of Mathematics, National University of Mexico, Blvd. Juriquilla, 3001 Queretaro, Mexico.
*Corresponding author: cesar@im.unam.mx

arterial models have been studied in [40]. However, 3D simulations are computationally expensive and are often not a practical tool for a timely evaluation before a surgical treatment. This has motivated the development of 1D models which reasonably well describe the propagation of pressure waves in arteries [12]. A 1D hyperbolic model for compliant axi-symmetric idealized vessels is derived in [6] and the properties of the model are discussed. The analysis of the blood flow after an endovascular repair is studied in [5], in which case the PDE based model has discontinuous coefficients. Furthermore, effects of viscous dissipation, viscosity of the fluid and other two-dimensional effects were incorporated in a "one-and-a-half dimensional" model in [7], where it is not necessary to prescribe an axial velocity profile *a priori*. In [8], a coupled model that describes the interaction between a shell and a mesh-like structure is derived. The structure consists of 3D mesh-like elastic objects and the model embodies a 2D shell model and a 1D network model. Well-balanced high-order numerical schemes for one-dimensional (1D) blood flow models are constructed in [30] using the Generalized Hydrostatic Reconstruction technique. Path-conservative finite volume schemes based on the DOT Riemann solver in the context of computational hemodynamics has been developed in [29] and a generalization to flexible visco-elastic tubes with compressible flows in [27]. Arbitrary Accuracy Derivative (ADER) finite volume methods for hyperbolic balance laws with stiff terms are extended to solve 1D blood flows for viscoelastic vessels in [28], and such technique is applied to analyze the treatment of viscoelastic effects at junctions in [31]. The effects of variations of the mechanical properties of arteries due to diseases such as stenosis or aneurysms have also being studied using 1D models [21, 38, 39]. It has also been noted in [18] that 1D models are able to describe the fluid's evolution after arteriovenous fistula (AVF) surgeries in 6 out of 10 patients and selected the same AVF location as an experienced surgeon in 9 out of 10 patients. See also [19] for a comparison with experimental data using 1D models. Although 1D models have shown to be a reasonably good approximation in many situations, there exist limitations due in part to simplifications such as axial symmetry. The cross section is assumed to be a circle, which could impact the accuracy of the model's prediction.

The contributions listed above consider the two extreme cases where the models are either 3D or 1D, and some interactions between them. Two-dimensional (2D) models are a good balance that provides more realistic results compared to its 1D counterparts with the advantage of a low computational cost when compared to the 3D models. There has been some efforts in that direction. For instance, a blood flow model that takes into account axial and radial displacements is derived in [9]. The model in [9] considers a radial velocity that adjusts to the axial velocity by the continuity equation. Although it provides detailed information about the velocity that extends in the radial direction (2D), it is still restricted by the axi-symmetric assumptions. The model presented in [10] can be considered intermediate between 3D and 1D for general cross-sections in the sense that the equations are written in terms of the area A without specifying whether the cross section is axi-symmetric (circular), ellipsoidal or something else.

In this work, we derive an intermediate 2D model where any shape of the cross section can be considered while maintaining a still much lower computational cost compared to 3D simulations. The derivation and implementation of a model in two dimensions is one of our main contributions. The model is derived using asymptotic analysis that follows certain physical considerations. The velocity and vessel's radius here depend on the cross section's angle and axial position, while the 1D counterpart considers a uniform radius that varies only in the axial direction. Our model can handle perturbations and variations in the wall's elasticity affecting any specific area of the vessel while 1D simulations can only consider perturbations affecting entire cross sections. This is relevant in simulations of diseases such as aneurysms and stenosis that involve vessels with walls that have damaged areas, not necessarily entire cross sections. Furthermore, we present the properties of the model, construct a well-balanced central-upwind scheme and include numerical tests that show its merits. It is well known that 1D models can accurately capture pulse pressure waves [38]. The 2D model that we present here can also capture the wall deformation due to those waves propagating throughout the vessel and its variations in the angular direction as a response to the wall's elasticity properties. There exist other scenarios where 2D models can offer useful information. For instance, stress-strain responses in a vessel are of particular interest in distinct studies [1]. Such relation could also vary in the angular momentum in a vessel with asymmetric elasticity properties and this 2D model can capture such imbalances more accurately. Even velocity field patterns have

been of interest in multiphase hemodynamics [20]. In our setting, vortex-like structures have been observed in simulations of vessels with asymmetric elasticity properties, which would not be possible to identify in 1D models. In contrast with the model in [9], our cross sections can evolve freely into any shape as a response to the fluids discharge, transmural pressure, and the wall's elasticity properties. Such dynamics are dictated by the leading order contributions resulting from the asymptotic analysis and the average process. On the other hand, the review article [33] discusses multiscale approaches for the numerical simulation of blood flow problems. It couples different scales going from centimeters (singular vascular district) to meters (entire network), using models with different complexities from lumped parameters (0D) to 1D, 2D and 3D systems. The 2D model implemented in the multiscale approach considers only radial displacements. On the contrary, the model in our work takes radial averages and allows for variations in the angular direction. We believe our model can serve as a complement to provide useful information in scenarios where variations in the angular directions are important. A systematic comparison between 3D and 1D models models can also be found in [40], showing good agreement. The 2D model in this work can provide additional details as described above.

Our work is organized as follows. Section 2 provides the derivation of the system of partial differential equations that describes our model, leaving the details of the asymptotic expansion to Appendix A. The model is derived by applying asymptotic analysis to a system of equations that takes into account Fluid-Structure interactions through the Navier-Stokes equations in a moving domain and an elastic membrane. See more about Fluid-Structure interactions in, *e.g.*, [14,16]. The equations are written in cylindrical coordinates and we proceed by integrating in the radial direction in each cross section. Section 3 describes the quasilinear properties of the model, where we show that the system is conditionally hyperbolic. A closed form of the transmural pressure term is presented. Section 4 focuses on the description of the positivity-preserving well-balanced second-order central-upwind scheme. Finally, in Section 5 we test our model by considering a variety of numerical experiments.

2. Derivation of the model

2.1. The geometry of the vessel

The model presented here is derived by computing the radial average in each axial position and angle in the vessel's cross section. Although it can be easily generalized, let us assume for simplicity that the vessel is aligned in the $x-z$ plane and that it extends along a curve that passes through each cross section. The parametrization of such curve is assumed to be known and its location is then represented by its arclength's position s and coordinates $(x_o(s), y_o = 0, z_o(s))$. Each cross section is identified with the arclength position s of the curve intersecting it. Any position in each cross section is located with the angle θ formed between the displacement from the intersection and a reference vector. The variables and parameters are functions of the axial position s and angle θ. As a result, the model allows for arbitrary cross sections and variations in each angle θ, resulting in a 2D model.

The above parametrization is done such that $s = 0$ corresponds to the left end of the vessel while $s = s_L$ is related to the right end. For each s, the cross-section denoted by $C(s)$ is contained in a plane passing through $(x_o(s), y_o = 0, z_o(s))$ and perpendicular to the unit tangent vector $\mathbf{T}(s) = (\cos(\alpha(s)), 0, \sin(\alpha(s)))$. Here $\alpha(s)$ is the angle of the curve with respect to the horizontal axis x. Furthermore, for a point (x, y, z) in the cross-section $C(s)$, let θ be the angle between the normal vector $(-\sin(\alpha(s)), 0, \cos(\alpha(s)))$ and the displacement $(x, y, z) - (x_o(s), 0, z_o(s))$. This gives the following change of variables:

$$\begin{aligned} x(r, s, \theta) &= x_o(s) - r\sin(\alpha(s))\sin(\theta), \\ y(r, s, \theta) &= r\cos(\theta), \\ z(r, s, \theta) &= x_o(s) + r\cos(\alpha(s))\sin(\theta), \end{aligned} \tag{1}$$

where r is the norm of the displacement. The corresponding Jacobian is given by

$$|J| = r(1 - r\sin(\theta)\alpha'(s)).$$

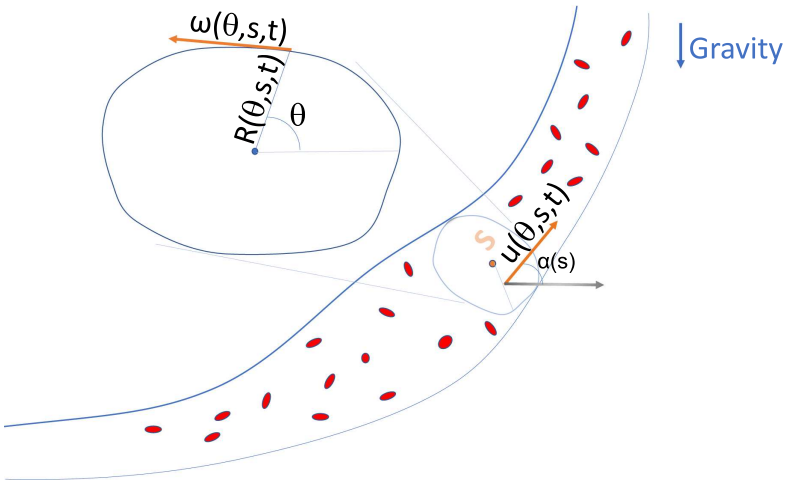

FIGURE 1. Symbolic representation of model for blood flows passing through a compliant vessel. Each cross section is described by a radius $R(\theta, s, t)$ that varies in the angular direction θ but it can also depend on s and t. The axial and angular velocities are represented by u and ω. Here, $\alpha(s)$ is the angle between the axial vessel's direction at arclength position s with the horizontal axis.

A sufficient condition for the change of variables to be valid is that the radius r for any point in the cross section does not exceed the radius of curvature of the parametrization. That is,

$$r \leq \mathfrak{R}(s) = \frac{1}{\kappa(s)},$$

where $\kappa(s) = |\alpha'(s)|$ is the vessel's curvature and $\mathfrak{R}$ is the radius of curvature. This is a very reasonable assumption, even in the case of an stenosis, specially if it happens in an area with zero curvature.

Figure 1 shows the symbolic representation of the model to be derived below. The vessel's radius may vary as a function of angle, axial position and time, $R = R(t; \theta, s)$. As a result, the vessel may have any cross-sectional shape. On the contrary, one-dimensional models assume a uniform radius, independent of θ, restricting the cross section to be axi-symmetric.

2.2. The averaged leading order equations

The derivation of the model requires rewriting the equations in cylindrical coordinates and carry out an asymptotic analysis to determine the leading order contribution under the following assumptions. In this section, we denote the density by ρ and $V_c = (V_s, V_r, V_\theta)$ is the vector of axial, radial and angular velocities in cylindrical coordinates. Let $V_{s,o}$, $V_{r,o}$, and $V_{\theta,o}$ be the corresponding characteristic scales. Let also λ and R_o be the characteristic axial and radial lengthscales. The small parameter in this expansion is the ratio between radial and axial lengthscales

$$\epsilon := \frac{R_o}{\lambda} = \frac{V_{r,o}}{V_{s,o}}. \tag{2}$$

Typical values in the aorta between the renal and the iliac arteries gives $\epsilon \approx 10^{-2}$ [6]. Furthermore, we assume that the gravity g, the scales of pressure ($[P]$), radius (R_o), time (T), axial and linear angular velocities ($V_{s,o}, V_{\theta,o}$) satisfy

$$\frac{[P]}{\rho_o V_{s,o}^2} = O(1), \quad \frac{V_{s,o}}{R_o V_{\theta,o}} = O(1), \quad \frac{gT}{V_{s,o}} = O(1). \tag{3}$$

Under these assumptions, the acceleration of gravity is comparable to the characteristic acceleration of the system in the axial direction. This is reasonable for typical velocities of order $O(1\ \mathrm{ms}^{-1})$ and a timescale of $T = 0.1$ s. On the other hand, the change of variables is valid provided that $r|\alpha'(s)| < 1$. As a stronger assumption, we assume that $r\alpha'(s)$ is small, which implies that the artery's radius of curvature is large compared to its cross-sectional radius. On the other hand, an approximate value for blood viscosity in arteries can be taken as a constant $\nu = 4$ cP $= 4 \times 10^{-2}$ g (s cm)$^{-1}$ [21]. Using $\rho_o = 1050$ kg m^{-3}, and $R_o = 0.82$ cm, it gives us $\frac{\nu T}{\rho_o R_o^2} = 0.56 \times 10^{-2}$. Based on this estimation, we assume

$$R_o|\alpha'(s)| = O(\epsilon), \quad \text{and} \quad \frac{\nu T}{\rho_o R_o^2} = O(\epsilon). \tag{4}$$

After removing terms of order $O(\epsilon^2)$ in the non-dimensionalized equations, we obtain

$$\begin{aligned}
|J|\tfrac{D}{Dt}(\rho) &= 0,\\
|J|\tfrac{D}{Dt}\left(\rho\left[\tfrac{|J|}{r}\right]^2 V_s\right) &= r\left[\tfrac{|J|}{r}\right]^2 \partial_s\left(\tfrac{|J|}{r}\right)\rho V_s^2 - |J|\partial_s(p) - |J|\sin(\alpha(s))\rho g\\
&\quad +\nu\partial_r\left(|J|\partial_r\left(\left[\tfrac{|J|}{r}\right]^2 V_s\right)\right),\\
|J|\tfrac{D}{Dt}\left(\rho r^2 V_\theta\right) &= r\left[\tfrac{|J|}{r}\right]^2 \partial_\theta\left(\tfrac{|J|}{r}\right)\rho V_s^2 - |J|\partial_\theta(p)\\
&\quad +\nu\partial_r\left(|J|\left[\partial_r\left(r^2 V_\theta\right) - 2rV_\theta\right]\right),\\
\nabla_c\cdot(|J|\mathbf{V}_c) &= 0.
\end{aligned} \tag{5}$$

The radial averaging is applied to the limiting equations. The details of the reduction of the system are left to Appendix A.

2.3. The main system

Let $R(s,\theta,t)$ denote the vessel's cross-sectional radius at each position s, angle θ and time t. Let us define

$$A(R,s,\theta,t) = \int_0^R |J|\mathrm{d}r, \qquad u(s,\theta,t) = \frac{1}{A}\int_0^R V_s|J|\mathrm{d}r, \tag{6}$$

$$\omega(s,\theta,t) = \frac{1}{A}\int_o^R V_\theta|J|\mathrm{d}r, \quad \text{and} \quad L(R,s,\theta,t) = \frac{1}{A}\int_o^R r^2 V_\theta|J|\mathrm{d}r, \tag{7}$$

where

$$A = A(R,s,\theta) = \frac{R^2}{2} - \frac{R^3}{3}\sin(\theta)\alpha'(s)$$

is the radially integrated Jacobian. On the other hand, u, ω and L are the radially-averaged axial velocity, angular velocity and angular momentum, respectively.

The model is derived after an integration in the radial direction, assuming a streamline condition

$$[V_r]_{r=R} = \partial_t(R) + [V_s]_{r=R}\partial_s(R) + [V_\theta]_{r=R}\partial_\theta(R)$$

at the artery's wall and a slowly varying density, which is approximated by a constant value. The main system is

$$\begin{aligned}
\partial_t(A) + \partial_s(A\,u) + \partial_\theta(A\,\omega) &= 0,\\
\partial_t(\psi_{s,o}Au) + \partial_s\big(\psi_{s,1}Au^2\big) + \partial_\theta(\psi_{s,2}Au\omega) &= -A\partial_s\Big(\tfrac{p}{\rho}\Big) - gA\sin(\alpha(s))\\
&\quad + \textstyle\int_o^R r\Big[\frac{|J|}{r}\Big]^2\partial_s\Big(\frac{|J|}{r}\Big)V_s^2\mathrm{d}r\\
&\quad + \tfrac{\nu}{\rho}\Big(|J|\partial_r\Big(\Big[\tfrac{|J|}{r}\Big]^2V_s\Big)\Big)\big|_o^R,\\
\partial_t(AL) + \partial_s(\psi_{\theta,1}ALu) + \partial_\theta(\psi_{\theta,2}AL\omega) &= -A\partial_\theta\Big(\tfrac{p}{\rho}\Big)\\
&\quad + \textstyle\int_o^R r\Big[\frac{|J|}{r}\Big]^2\partial_\theta\Big(\frac{|J|}{r}\Big)V_s^2\mathrm{d}r\\
&\quad + \tfrac{\nu}{\rho}\big(|J|\big[\partial_r(r^2V_\theta) - 2rV_\theta\big]\big)\big|_o^R,
\end{aligned} \tag{8}$$

where $\psi_{s,o}, \psi_{s,1}, \psi_{s,2}, \psi_{\theta,1}$ and $\psi_{\theta,2}$ are Coriolis terms satisfying

$$\begin{aligned}
\psi_{s,o}Au &= \int_o^R |J|\left[\frac{|J|}{r}\right]^2 V_s\mathrm{d}r,\\
\psi_{s,1}Au^2 &= \int_o^R |J|\left[\frac{|J|}{r}\right]^2 V_s^2\mathrm{d}r, \qquad \psi_{s,2}Au\omega = \int_o^R |J|\left[\frac{|J|}{r}\right]^2 V_sV_\theta\mathrm{d}r,\\
\psi_{\theta,1}ALu &= \int_o^R |J|r^2V_\theta V_s\mathrm{d}r, \qquad \psi_{\theta,2}AL\omega = \int_o^R |J|r^2V_\theta^2\mathrm{d}r.
\end{aligned} \tag{9}$$

The angular velocity and angular momentum are related by

$$L = A_\theta\omega, \quad A_\theta = \frac{\int_o^R r^2V_\theta|J|\mathrm{d}r}{\int_o^R V_\theta|J|\mathrm{d}r}.$$

The integral of the Jacobian in the radial direction A is one of our conserved variables. This variable A satisfies that $\int_{s_0}^{s_1}\int_0^{2\pi} A\mathrm{d}\theta\mathrm{d}s$ is the volume in the corresponding artery's region. In the case of a circular cross section, the integral with respect to θ gives us the cross-sectional area. The balance of axial and angular momenta determine the other two conserved quantities, given by

$$Q_1 = \psi_{s,o}Au, \quad Q_2 = AL,$$

where $\psi_{s,o}$ takes into account the effect of curvature in the artery, and $\psi_{s,o} = 1$ for horizontal vessels. One still needs to determine a profile for the axial and angular velocities V_s and V_θ as functions of r to close the system. For a given profile, the non-dimensional Coriolis terms $\psi_{s,o}$, $\psi_{s,1}$, $\psi_{s,2}$, $\psi_{\theta,1}$ and $\psi_{\theta,2}$ are all explicit functions of A, s and θ. In fact, those parameters are explicit functions of $R\sin(\theta)\alpha'(s)$ for the profiles considered in this paper, and are therefore constant parameters for vessels with zero curvature. See Section 3.2 for more details. The transmural pressure, which is the pressure difference between the two sides of the artery's wall is denoted by p. The elasticity properties of the vessel are determined by a relationship between p, the area A and possibly the variables s and θ due to non-uniform properties in the artery (explicit dependance on parameters). That is, we assume that the transmural pressure is an explicit function

$$p = p(A, s, \theta). \tag{10}$$

This way, the interaction of the fluid with the 2D membrane is parametrized with the use of a suitable vessel law that relates the transmural pressure p with the area A. Furthermore, we assume that the transmural pressure vanishes at a given state at rest $A_o = A_o(s,\theta) = \frac{R_o^2}{2} - \frac{R_o^3}{3}\sin(\theta)\alpha'(s)$ with $R_o = R_o(s,\theta)$ such that

$$p(A_o(s,\theta), s, \theta) = 0.$$

Some properties such as the hyperbolicity of the system are shown independently of the profiles, and we take equation (8) as the most general form of the system. This closes the system since everything is given in terms of the conserved quantities $A,\ Q_1$ and Q_2, and s, θ due to the presence of varying parameters.

Conservation form

The model can be written in conservation form. For that end, we need to introduce the following notation. The transmural pressure and other parameters such as the Coriolis terms are explicit functions $q = q(A,\ s,\ \theta)$ of A, s and θ. On the other hand, model parameters such as R_o and A_o depend explicitly on (s, θ). We will denote by $\partial_1,\ \partial_2,\ \partial_3$ the derivatives with respect to A, s and θ, keeping the other terms fixed. Thus

$$\partial_s(p(A(s,\theta,t),s,\theta)) = \partial_1 p\,\partial_s A + \partial_2 p,\ \partial_\theta(p(A(s,\theta,t),s,\theta)) = \partial_1 p\,\partial_\theta A + \partial_3 p. \tag{11}$$

We distinguish them from ∂_s and ∂_θ, which take into account the variations of the conserved variables with respect to s and θ over time.

In order to get the conservation form, we define the splitting of the transmural pressure as

$$p = \widehat{p} + \overline{p}, \tag{12}$$

where

$$\widehat{p}(A,s,\theta) = \frac{1}{A}\int_{A_o}^{A} \mathcal{A}\partial_1(p(\mathcal{A},s,\theta))\mathrm{d}\mathcal{A}, \tag{13}$$

which satisfy

$$\begin{aligned} A\partial_s(p) &= \partial_s(A\widehat{p}) + A\partial_2\overline{p} \quad \text{and} \\ A\partial_\theta(p) &= \partial_\theta(A\widehat{p}) + A\partial_3\overline{p}. \end{aligned} \tag{14}$$

In the decomposition (13), $\mathcal{A}$ is used to denote an integration variable.

The 2D model for blood flows in arteries with arbitrary cross sections is written as a hyperbolic system of balance as

$$\partial_t \mathbf{U} + \partial_s\,\mathbf{F}(\mathbf{U}) + \partial_\theta\,\mathbf{G}(\mathbf{U}) = S(\mathbf{U}), \tag{15}$$

where

$$\mathbf{U} = \begin{pmatrix} A \\ \psi_{s,o}Au \\ AL \end{pmatrix}, \quad \mathbf{F}(\mathbf{U}) = \begin{pmatrix} Au \\ \psi_{s,1}Au^2 + \frac{1}{\rho}A\widehat{p} \\ \psi_{\theta,1}AuL \end{pmatrix}, \quad \mathbf{G}(\mathbf{U}) = \begin{pmatrix} A\omega \\ \psi_{s,2}Au\,\omega \\ \psi_{\theta,2}AL\,\omega + \frac{1}{\rho}A\widehat{p} \end{pmatrix} \tag{16}$$

are the vectors of conserved variables and the fluxes in the axial and angular directions, respectively. The vector of source terms is

$$\mathbf{S}(\mathbf{U}) = \begin{pmatrix} 0 \\ -\frac{A}{\rho}\partial_2\overline{p} - A\sin(\alpha(s))g + \int_o^R \frac{|J|}{r}\partial_s\left(\frac{|J|}{r}\right)V_s^2|J|\mathrm{d}r + \frac{\nu}{\rho}\left[|J|\partial_r\left(\left[\frac{|J|}{r}\right]^2 V_s\right)\right]_{r=R} \\ -\frac{A}{\rho}\partial_3\overline{p} + \int_o^R \frac{|J|}{r}\partial_\theta\left(\frac{|J|}{r}\right)V_s^2|J|\mathrm{d}r + \frac{\nu}{\rho}\left[|J|\partial_r\left(r^2 V_\theta\right) - 2r|J|V_\theta\right]_{r=R} \end{pmatrix}. \tag{17}$$

We note that none of the source terms are non-conservative products. The source terms only involve derivatives of the model parameters with respect to the explicit dependance on (s, θ) and no derivates of the solution itself are present. This prevents both theoretical and numerical complications when shockwaves arise. Below we show explicit expressions of the source and Coriolis terms for a particular choice of profiles for the transmural pressure, axial and angular velocities. As we will see, the expressions are very simple in the case of horizontal arteries ($\alpha'(s) = 0$).

System (16) is valid for a general vessel law where p is a function of A but it could also depend explicitly on the independent variables s and θ when the vessel law involves variable coefficients. As we will see below,

the pressure must be increasing with respect to A in order to guarantee hyperbolicity. Besides that and the restriction that the transmural pressure vanishes at a state of rest, the aforementioned vessel law is very general. The pressure decomposition in equation (13) is used to write the system as a balance law where the source terms do not involve non-conservative products (important for weak solutions), and it is valid for the general vessel law.

3. Properties of the model

3.1. Hiperbolicity of the model

The conservation form in equation (15) is crucial because it allows us to formulate the Rankine–Hugoniot conditions for weak solutions in the presence of shockwaves. We can apply the theory of weak solutions provided the model is hyperbolic. The hyperbolic properties of system (15) can be studied through its quasilinear formulation, which is given by

$$\partial_t \mathbf{U} + M_s(\mathbf{U})\partial_s \mathbf{U} + M_\theta(\mathbf{U})\partial_\theta \mathbf{U} = \tilde{\mathbf{S}}(\mathbf{U}), \tag{18}$$

where the coefficient matrices are

$$M_s(\mathbf{U}) = \begin{pmatrix} -\frac{A}{\psi_{s,o}}\partial_1(\psi_{s,o})u & \frac{1}{\psi_{s,o}} & 0 \\ \frac{1}{\rho}\partial_1(A\widehat{p}) - \left(\frac{\psi_{s,1}}{\psi_{s,o}}\right)^2 \partial_1\left(\frac{\psi_{s,o}^2 A}{\psi_{s,1}}\right)u^2 & 2\frac{\psi_{s,1}}{\psi_{s,o}}u & 0 \\ -\frac{\psi_{\theta,1}^2}{\psi_{s,o}}\partial_1\left(\frac{\psi_{s,o}A}{\psi_{\theta,1}}\right)uL & \frac{\psi_{\theta,1}}{\psi_{s,o}}L & \psi_{\theta,1}u \end{pmatrix} \tag{19}$$

and

$$M_\theta(\mathbf{U}) = \begin{pmatrix} -\frac{A}{A_\theta}\partial_1(A_\theta)\omega & 0 & \frac{1}{A_\theta} \\ -\frac{\psi_{s,2}^2}{\psi_{s,o}A_\theta}\partial_1\left(\frac{\psi_{s,o}AA_\theta}{\psi_{s,2}}\right)u\omega & \frac{\psi_{s,2}}{\psi_{s,o}}\omega & \frac{\psi_{s,2}}{A_\theta}u \\ \frac{1}{\rho}\partial_1(A\widehat{p}) - \psi_{\theta,2}^2\partial_1\left(\frac{AA_\theta}{\psi_{\theta,2}}\right)\omega^2 & 0 & 2\psi_{\theta,2}\omega \end{pmatrix}. \tag{20}$$

The vector of source terms of the quasi-linear formulation is

$$\tilde{S}(\mathbf{U}) = S(\mathbf{U}) + \begin{pmatrix} \frac{A}{\psi_{s,o}}\partial_2(\psi_{s,o})u + \frac{A}{A_\theta}\partial_3(A_\theta)\omega \\ -\frac{1}{\rho}\partial_2(A\widehat{p}) + \left(\frac{\psi_{s,1}}{\psi_{s,o}}\right)^2\partial_2\left(\frac{\psi_{s,o}^2 A}{\psi_{s,1}}\right)u^2 + \frac{\psi_{s,2}^2}{\psi_{s,o}A_\theta}\partial_3\left(\frac{\psi_{s,o}AA_\theta}{\psi_{s,2}}\right)u\omega \\ -\frac{1}{\rho}\partial_3(A\widehat{p}) + \frac{\psi_{\theta,1}^2}{\psi_{s,o}}\partial_2\left(\frac{\psi_{s,o}A}{\psi_{\theta,1}}\right)uL + \psi_{\theta,2}^2\partial_3\left(\frac{AA_\theta}{\psi_{\theta,2}}\right)\omega^2 \end{pmatrix}. \tag{21}$$

The matrices M_s and M_θ have two null entries in one column and their eigenvalues have explicit expressions given by

$$\lambda_o^s = \psi_{\theta,1}u, \quad \lambda_\pm^s = \frac{2\psi_{s,1} - A\partial_1(\psi_{s,o})}{2\psi_{s,o}}u \pm \sqrt{\frac{\frac{1}{\rho}\partial_1(A\widehat{p})}{\psi_{s,o}} + \Upsilon_1 u^2} \tag{22}$$

for M_s, and

$$\lambda_o^\theta = \frac{\psi_{s,2}}{\psi_{s,o}}\omega, \qquad \lambda_\pm^\theta = \frac{2\psi_{\theta,2}A_\theta - A\partial_1(A_\theta)}{2A_\theta}\omega \pm \sqrt{\frac{\frac{1}{\rho}\partial_1(A\widehat{p})}{A_\theta} + \Upsilon_2\omega^2} \tag{23}$$

for M_θ, respectively. Here,

$$\begin{aligned} \Upsilon_1 &= \frac{1}{\psi_{s,o}^2}\left[\psi_{s,1} - \frac{1}{2}A\partial_1(\psi_{s,o})\right]^2 + \frac{1}{\psi_{s,o}}[A\partial_1(\psi_{s,1}) - \psi_{s,1}], \quad \text{and} \\ \Upsilon_2 &= \frac{1}{A_\theta^2}\left[\psi_{\theta,2}A_\theta - \frac{1}{2}A\partial_1(A_\theta)\right]^2 + \frac{1}{A_\theta}[A\partial_1(\psi_{\theta,2}A_\theta) - \psi_{\theta,2}A_\theta] \end{aligned} \tag{24}$$

are all non-dimensional quantities.

Below we specify the profiles for the axial and angular velocities. For those specific profiles, we show that $\Upsilon_1 = \Upsilon_1(\Gamma)$ and $\Upsilon_2 = \Upsilon_2(\Gamma)$ are explicit rational functions of Γ, where

$$\Gamma = R\sin(\theta)\alpha'(s). \tag{25}$$

Such functions satisfy $\Upsilon_1(\Gamma = 0) = \psi_{s,1}(\psi_{s,1} - 1)$ and $\Upsilon_2(\Gamma = 0) = \left(\psi_{\theta,2} - \frac{1}{2}\right)^2$. The special case $\Gamma = 0$ corresponds to a horizontal vessel.

Proposition 1. *Let us assume that p is strictly increasing with respect A, with positive partial derivative, except possibly at $A = 0$ where the vessel collapses. The coefficient matrices M_s and M_θ given by (19) and (20) have real eigenvalues and a complete set of eigenvectors, subject to the conditions $0 < R < \frac{1}{|\alpha'(s)|}$, and $\Upsilon_1, \Upsilon_2 \geq 0$.*

The condition $0 < R < \frac{1}{|\alpha'(s)|}$ indicates that the artery's radius must not exceed the artery's radius of curvature and it is required for the change of variables to cylindrical coordinates to be valid. This implies that the non-dimensional parameter Γ satisfies $|\Gamma| \leq 1$. For specific profiles used in this paper for the axial and angular velocities, Υ_1 and Υ_2 are in fact non negative for $\Gamma \in [-1, 1]$.

Proof. Under the above hypothesis, and the fact that

$$\partial_1(A\hat{p}) = A\partial_1 p \geq 0$$

the expressions inside the square roots in equations (22) and (23) are non negative. As a result, all the eigenvalues are real. The expressions inside the square roots could only vanish if $A = 0$ (or equivalently $R = 0$). It would also require that $u = 0$ or $\omega = 0$ if $\Upsilon_1 = 0$ or $\Upsilon_2 = 0$ respectively. This could happen for certain parameter choices, specially in horizontal vessels. In any case, the condition $R > 0$ is sufficient to guarantee that $\lambda^s_+ \neq \lambda^s_-$ and $\lambda^\theta_+ \neq \lambda^\theta_-$. However, the eigenvalue λ^s_o may still have multiplicity 2 if it coincides with λ^s_+ or λ^s_-. And the same applies for the matrix M_θ.

In the case when the eigenvalues for M_s are different and writing $M_s = (a_{ij})$, the eigenvectors form a basis and are given by

$$\mathbf{v}^s_o = \begin{pmatrix} 0 \\ 0 \\ 1 \end{pmatrix}, \quad \mathbf{v}^s_\pm = \begin{pmatrix} a_{12} \\ \lambda^s_\pm - a_{11} \\ \frac{(a_{11} - \lambda^s_\pm)a_{32} - a_{12}a_{31}}{a_{33} - \lambda^s_\pm} \end{pmatrix}.$$

If $\lambda^s_o = \lambda^s_-$, the eigenvectors are given by

$$\mathbf{v}^s_o = \begin{pmatrix} 0 \\ 0 \\ 1 \end{pmatrix}, \quad \mathbf{v}^s_- = \begin{pmatrix} a_{12} \\ \lambda^s_- - a_{11} \\ 0 \end{pmatrix}, \quad \mathbf{v}^s_+ = \begin{pmatrix} a_{12} \\ \lambda^s_+ - a_{11} \\ \frac{(a_{11} - \lambda^s_+)a_{32} - a_{12}a_{31}}{a_{33} - \lambda^s_+} \end{pmatrix}.$$

Since $\lambda^s_+ \neq \lambda^s_-$, one can easily check that the eigenvectors form a complete basis because $a_{12} = \frac{1}{\psi_{s,o}} > 0$.

The case $\lambda^s_o = \lambda^s_+$ and the analysis for M_θ are analogous, which concludes the proof. □

The hyperbolicity of the model requires that $n_s M_s + n_\theta R_o M_\theta$ has real eigenvalues and a complete set of eigenvectors for all $n_s, n_\theta \in \mathbb{R}$ such that $n_s^2 + n_\theta^2 = 1$. Here R_o is a constant in units of length that appears due to the fact that s and θ have different units. For the general case, the matrix $n_s M_s + n_\theta R_o M_\theta$ has not a simple form. However, one can easily analyze the special case of a horizontal vessel ($\alpha'(s) = 0$) and $\omega = 0$. In such case, $\psi_{s,o},\ \psi_{s,1},\ \psi_{s,2},\ \psi_{\theta,1}$ are all constant, and the characteristic polynomial is

$$P(\lambda) = -\lambda^3 + c_2\lambda^2 + c_1\lambda + c_o,$$

where

$$
\begin{aligned}
c_2 &= (2\psi_{s,1} + \psi_{\theta,1}) u n_s, \\
c_1 &= \frac{1}{\rho}\partial_1(A\hat{p})\left(n_s^2 + \frac{R_o^2}{A_\theta} n_\theta^2\right) + (-\psi_{s,1} - 2\psi_{s,1}\psi_{\theta,1})\, u^2\, n_s^2, \\
c_o &= \left[-\frac{1}{\rho}\partial_1(A\hat{p}) + \psi_{s,1} u^2\right] \psi_{\theta,1}\, n_s^3\, u \\
&\quad + \frac{1}{\rho}\partial_1(A\hat{p}) \frac{R_o^2}{A_\theta} (-2\psi_{s,1} + \psi_{s,2})\, n_\theta^2\, u\, n_s.
\end{aligned}
$$

Using Cardano's approach, we know the characteristic polynomial has three distinct real eigenvalues if

$$
\begin{aligned}
0 &< -27c_o^2 - 18c_2c_1c_o + 4c_1^3 - 4c_2^3c_o + c_2^2c_1^2 \\
&= 4\left(\frac{1}{\rho}\partial_1(A\hat{p}) + \psi_{s,1}(\psi_{s,1} - 1)u^2\right)\left[\frac{1}{\rho}\partial_1(A\hat{p}) + (2\psi_{s,1}\psi_{\theta,1} - \psi_{s,1} - \psi_{\theta,1}^2)u^2\right]^2 n_s^6 \\
&\quad + 12\frac{\left(\frac{1}{\rho}\partial_1(A\hat{p})\right)^3 R_o^2}{A_\theta} n_s^4 n_\theta^2 \\
&\quad + 4\frac{\left(\frac{1}{\rho}\partial_1(A\hat{p})\right)^2 R_o^2 u^2}{A_\theta}\big(20\psi_{s,1}^2 + \psi_{\theta,1}(9\psi_{s,2} + 5\psi_{\theta,1}) - \psi_{s,1}(6 + 9\psi_{s,2} + 19\psi_{\theta,1})\big) n_s^4 n_\theta^2 \\
&\quad + 4\frac{\frac{1}{\rho}\partial_1(A\hat{p}) R_o^2 u^4}{A_\theta}\big[16\psi_{s,1}^4 - \psi_{s,2}\psi_{\theta,1}^3 - 4\psi_{s,1}^3(5 + 2\psi_{s,2} + 4\psi_{\theta,1}) \\
&\qquad\qquad + \psi_{s,1}\psi_{\theta,1}[3\psi_{s,2}(-3 + \psi_{\theta,1}) + (-5 + \psi_{\theta,1})\psi_{\theta,1}] \\
&\qquad\qquad + \psi_{s,1}^2(3 + \psi_{\theta,1}(19 + 2\psi_{\theta,1}) + \psi_{s,2}(9 + 6\psi_{\theta,1}))\big] n_s^4 n_\theta^2 \\
&\quad + 12\frac{\left(\frac{1}{\rho}\partial_1(A\hat{p})\right)^3 R_o^4}{A_\theta^2} n_s^2 n_\theta^4 \\
&\quad + \frac{\left(\frac{1}{\rho}\partial_1(A\hat{p})\right)^2 R_o^4}{A_\theta^2} u^2\big[-32\psi_{s,1}^2 - 27\psi_{s,2}^2 - 18\psi_{s,2}\psi_{\theta,1} + \psi_{\theta,1}^2 \\
&\qquad\qquad + 4\psi_{s,1}(-3 + 18\psi_{s,2} + 4\psi_{\theta,1})\big] n_s^2 n_\theta^4 \\
&\quad + 4\frac{\left(\frac{1}{\rho}\partial_1(A\hat{p})\right)^3 R_o^6}{A_\theta^3} n_\theta^6.
\end{aligned}
$$

A sufficient condition for hyperbolicity is then

$$
\begin{aligned}
&\psi_{s,1} > 1, \\
&20\psi_{s,1}^2 + \psi_{\theta,1}(9\psi_{s,2} + 5\psi_{\theta,1}) - \psi_{s,1}(6 + 9\psi_{s,2} + 19\psi_{\theta,1}) && > 0, \\
&16\psi_{s,1}^4 - \psi_{s,2}\psi_{\theta,1}^3 - 4\psi_{s,1}^3(5 + 2\psi_{s,2} + 4\psi_{\theta,1}) \\
&\qquad + \psi_{s,1}\psi_{\theta,1}[3\psi_{s,2}(-3 + \psi_{\theta,1}) + (-5 + \psi_{\theta,1})\psi_{\theta,1}] \\
&\qquad + \psi_{s,1}^2(3 + \psi_{\theta,1}(19 + 2\psi_{\theta,1}) + \psi_{s,2}(9 + 6\psi_{\theta,1})) && > 0, \\
&-32\psi_{s,1}^2 - 27\psi_{s,2}^2 - 18\psi_{s,2}\psi_{\theta,1} + \psi_{\theta,1}^2 + 4\psi_{s,1}(-3 + 18\psi_{s,2} + 4\psi_{\theta,1}) && > 0.
\end{aligned}
$$

We have verified that such condition is met when we use the specific profiles and parameter values in Section 3.2. Although the hyperbolicity has been proved for the special case of horizontal vessels with vanishing angular

velocity, we believe this property is satisfied in a much more general context because Proposition 1 shows that each coefficient matrix can be diagonalized.

3.2. Specific profiles of pressure, axial and angular velocities

Following [6], a generalized Hagen–Poiseuille profile is assumed for the axial velocity:

$$V_s = e_s V_s^\star u, \quad V_s^\star = \frac{r}{|J|}\Big[1-\Big(\frac{r}{R}\Big)^{\gamma_s}\Big], \tag{26}$$

where

$$e_s(A,s,\theta) = \frac{A}{\int_o^R V_s^\star(r,R)|J|\mathrm{d}r}\cdot$$

This profile vanishes at the artery's wall and it is strongest at the center. The exponent γ_s controls the transition from the center to the walls. Taking $\gamma_s = 9$, we get the effect of a Newtonian fluid [35]. On the other hand, we use a similar profile for the angular velocity,

$$V_\theta = e_\theta V_\theta^\star \omega, \quad V_\theta^\star = \Big[1-\frac{\gamma_\theta}{\gamma_\theta+1}\frac{r}{R}\Big]\Big(\frac{r}{R}\Big)^{\gamma_\theta-1}, \quad \text{where } e_\theta(A,s,\theta) = \frac{A}{\int_o^R V_\theta^\star(r,R)|J|\mathrm{d}r}\cdot \tag{27}$$

In the numerical simulations we take $\gamma_\theta = 2$. It satisfies that the linear velocity rV_θ vanishes at the center and $\partial_r(rV_\theta) = 0$ at $r = R$. These gives:

$$\begin{aligned}
\psi_{s,o} &= 1-\frac{4(\gamma_s+2)}{3(\gamma_s+3)}\Gamma+\frac{\gamma_s+2}{2(\gamma_s+4)}\Gamma^2,\\
\psi_{s,1} &= \frac{\gamma_s+2}{\gamma_s+1}\Big[1-\frac{2}{3}\Gamma\Big]\Big[1-\frac{2(2\gamma_s+2)(\gamma_s+2)}{3(2\gamma_s+3)(\gamma_s+3)}\Gamma\Big],\\
\psi_{s,2} &= \frac{\gamma_s+2}{\gamma_s}\Big[1-\frac{(\gamma_\theta+2)(2\gamma_\theta+\gamma_s+2)}{2(\gamma_\theta+\gamma_s+1)(\gamma_\theta+\gamma_s+2)}\Big]\frac{1-\frac{2}{3}\Gamma}{1-\frac{2\gamma_\theta+3}{2(\gamma_\theta+3)}\Gamma}\times\\
&\quad\Big[1-\frac{2(\gamma_\theta+\gamma_s+1)\big(3\gamma_\theta^2+2\gamma_\theta\gamma_s+11\gamma_\theta+3\gamma_s+9\big)}{(\gamma_\theta+3)(\gamma_\theta+\gamma_s+3)(3\gamma_\theta+2\gamma_s+4)}\Gamma\\
&\quad+\frac{(\gamma_\theta+2)(\gamma_\theta+\gamma_s+1)(\gamma_\theta+\gamma_s+2)\big(3\gamma_\theta^2+2\gamma_s\gamma_\theta+15\gamma_\theta+4\gamma_s+16\big)}{(\gamma_\theta+3)(\gamma_\theta+4)(\gamma_\theta+\gamma_s+3)(\gamma_\theta+\gamma_s+4)(3\gamma_\theta+2\gamma_s+4)}\Gamma^2\Big],\\
\psi_{\theta,1} &= \frac{\gamma_s+2}{\gamma_s}\Big[1-\frac{(\gamma_\theta+3)(\gamma_\theta+4)(2\gamma_\theta+\gamma_s+4)}{2(\gamma_\theta+2)(\gamma_\theta+\gamma_s+3)(\gamma_\theta+\gamma_s+4)}\Big]\frac{1-\frac{2}{3}\Gamma}{1-\frac{(\gamma_\theta+3)(2\gamma_\theta+5)}{2(\gamma_\theta+2)(\gamma_\theta+5)}\Gamma},\\
\psi_{\theta,2} &= \frac{(\gamma_\theta+3)(\gamma_\theta+4)(5\gamma_\theta+6)}{16(\gamma_\theta+2)(2\gamma_\theta+3)}\frac{\big[1-\frac{2}{3}\Gamma\big]\Big[1-\frac{2\left(5\gamma_\theta^2+14\gamma_\theta+10\right)}{(2\gamma_\theta+5)(5\gamma_\theta+6)}\Gamma\Big]}{\Big[1-\frac{2\gamma_\theta+3}{2(\gamma_\theta+3)}\Gamma\Big]\Big[1-\frac{(\gamma_\theta+3)(2\gamma_\theta+5)}{2(\gamma_\theta+2)(\gamma_\theta+5)}\Gamma\Big]}, \text{ and}\\
A_\theta &= \frac{(\gamma_\theta+2)^2}{(\gamma_\theta+3)(\gamma_\theta+4)}\left[\frac{1-\frac{(\gamma_\theta+3)(2\gamma_\theta+5)}{2(\gamma_\theta+2)(\gamma_\theta+5)}\Gamma}{1-\frac{2\gamma_\theta+3}{2(\gamma_\theta+3)}\Gamma}\right]R^2.
\end{aligned}$$

The elasticity properties of the vessel can be described by the dependance of the transmural pressure on the radius A, and it must be an increasing function of A in order to maintain hyperbolicity. As discussed in [3], the elasticity properties of the vessel's wall may be impacted by the contraction of surrounding muscles or pathologies such as aneurysms, among others. Although deriving an explicit dependance $p = p(R,s)$ is complicated, valid

expressions can be found in [3, 30, 32]. Following [6], the numerical tests use the following expression of the transmural pressure,

$$p(A,s,\theta) = G_o(s,\theta)\left(\left(\frac{A}{A_o(s,\theta)}\right)^{\beta/2} - 1\right), \tag{28}$$

where $A_o = \frac{R_o^2}{2} - \frac{R_o^3}{3}\sin(\theta)\alpha'(s)$ as defined above. This includes the effect of the wall's thickness and the stress-strain response. Here, G_o is the elasticity coefficient. Shear stress is ignored, and it is assumed that the transmural pressure of the fluid is the only force exerted on the vessel's wall. The parameter $\beta > 1$ corresponds to a non-linear stress-strain response. The value $\beta = 2$ provides a good approximation for experimental data [6]. The dependance of G_o and R_o on s and θ allows us to explore the change in elasticity properties of the vessel's wall, or to explore the influence of vessel tapering on shock formation [5,12]. Here we adopt the parametrization of the elasticity parameter in terms of the Young's modulus and wall's thickness given by [40]

$$G_o(s,\theta) = \frac{4}{3}\frac{h_d}{r_d}E_Y, \tag{29}$$

where E_Y is the Young's modulus, $r_d(s,\theta)$ is the radius at diastolic pressure and $h_d(s,\theta)$ is the wall's thickness. In particular, the elasticity parameter $G_o(s,\theta)$ and the unstressed radius $R_o(s,\theta)$ can play the role of varying coefficients in the model. Such coefficients can be asymmetric across the axis in vessels that have non-uniform elasticity properties in damaged areas.

Taking (28), the corresponding explicit expressions of the transmural pressure decomposition in (12) are given by

$$\widehat{p}(A,s,\theta) = \frac{\beta}{\beta+2}p - \frac{\beta}{\beta+2}G_o\frac{A_o - A}{A}, \quad \overline{p}(A,s,\theta) = \frac{2}{\beta+2}p + \frac{\beta}{\beta+2}G_o\frac{A_o - A}{A}.$$

The source terms associated to the pressure are given by

$$\partial_2\overline{p} = \frac{\overline{p}}{G_o}\partial_2 G_o - \frac{\widehat{p}}{A_o}\partial_2 A_o, \quad \partial_3\overline{p} = \frac{\overline{p}}{G_o}\partial_3 G_o - \frac{\widehat{p}}{A_o}\partial_3 A_o. \tag{30}$$

Furthermore, the needed expressions to compute the source terms are given by

$$\begin{aligned}
\int_o^R r\partial_s\left(\frac{|J|}{r}\right)\left[\frac{|J|}{r}V_s\right]^2 \mathrm{d}r &= -\frac{8(\gamma_s+2)^2}{(\gamma_s+3)(2\gamma_s+3)}\left(\frac{A}{R}\right)^2 R\sin(\theta)\alpha''(s)u^2,\\
\int_o^R r\partial_\theta\left(\frac{|J|}{r}\right)\left[\frac{|J|}{r}V_s\right]^2 \mathrm{d}r &= -\frac{8(\gamma_s+2)^2}{(\gamma_s+3)(2\gamma_s+3)}\left(\frac{A}{R}\right)^2 R\cos(\theta)\alpha'(s)u^2,\\
\left[|J|\partial_r\left(\left[\frac{|J|}{r}\right]^2 V_s\right)\right]_{r=R} &= -(\gamma_s+2)[1-\Gamma]^2\frac{2A}{R^2}u,\\
\left[|J|\partial_r\left(r^2V_\theta\right) - 2|J|rV_\theta\right]_{r=R} &= -\frac{(\gamma_\theta+1)(\gamma_\theta+3)(\gamma_\theta+4)}{4(\gamma_\theta+2)}\left[\frac{1-\Gamma}{1-\frac{(\gamma_\theta+3)(2\gamma_\theta+5)}{2(\gamma_\theta+2)(\gamma_\theta+5)}\Gamma}\right]\frac{2A}{R^2}L.
\end{aligned}$$

It is important to note that the specific vessel law above is used for the numerical tests. However, equivalent expressions can be easily obtained for other scenarios. For instance, other expressions could be used to better approximate blood flows in collapsible tubes as it was done in [4,28].

3.3. Steady-States

Although transient flows provide a more complete description of pulsatile blood flows, it has been shown that under certain circumstances, steady states (*i.e.*, those independent of time) provide enough information for clinical assessment. In [13], a 5% difference was found in the time-averaged wall shear stress between transient

and steady states. There are, however, other clinical situations where transient flows are necessary for an accurate description of the pulsatile blood flow. In any case, our numerical scheme is constructed to accurately compute transient flows, including those near steady states.

The 2D model (15) admits a large class of steady states that arise when a delicate balance between flux gradients and source terms occurs. Here we characterize those steady states for vessels with zero curvature ($\alpha'(s) = 0$, or $\alpha = \alpha_o$ constant), and zero viscosity ($\nu = 0$) for fluids moving in the axial direction ($\omega = 0$). In those cases, equation (8) becomes

$$\begin{aligned} \partial_s(A\,u) &= 0, \\ \partial_s\left(\psi_{s,1} A u^2\right) &= -A\partial_s\left(\tfrac{p}{\rho}\right) - gA\sin(\alpha_o), \\ 0 &= -A\partial_\theta\left(\tfrac{p}{\rho}\right), \end{aligned}$$

which implies $Au = Q_1(\theta)$ is independent of s. The parameter $\psi_{s,1}$ is constant in vessels with zero curvature with the profiles in Section 3.2. The second equation for the balance of momentum can be re-written as

$$A\partial_s\left(\psi_{s,1}\frac{u^2}{2} + \frac{p}{\rho} + g z_o(s)\right) = 0,$$

where

$$z_o(s) = \sin(\alpha_o)\; s$$

is the artery's elevation above a reference height. As a result, smooth steady states for vessels with zero curvature, zero viscosity and vanishing angular velocity satisfy that the discharge $Q_1 = Au$ and the energy $E = \psi_{s,1}\frac{u^2}{2} + \frac{p}{\rho} + g z_o(s)$ are independent of s, whereas the transmural pressure p is independent of θ. In particular, one could have constant discharge and energy. The steady states at rest correspond to the special case

$$u = 0, \quad \omega = 0, \quad R = R_o(s,\theta), \quad \alpha(s) = 0. \tag{31}$$

Below we construct a numerical scheme that respects those steady states at rest for arteries with arbitrary cross sections.

4. Central-upwind numerical scheme

In this work, we use a central-upwind scheme, whose semi-discrete formulation is obtained after integrating equation (15) over each cell $\mathcal{C}_{j,k} := \left[s_{j-\frac{1}{2}}, s_{j+\frac{1}{2}}\right] \times \left[\theta_{k-\frac{1}{2}}, \theta_{k+\frac{1}{2}}\right]$, with center at (s_j, θ_k), $s_{j\pm\frac{1}{2}} = s_j \pm \Delta s/2$ and $\theta_{k\pm\frac{1}{2}} = \theta_k \pm \Delta\theta/2$. The cell averages $\overline{\mathbf{U}}_{j,k}(t)$

$$\overline{\mathbf{U}}_{j,k}(t) = \frac{1}{\Delta s \Delta\theta}\int_{\mathcal{C}_{j,k}}\int \mathbf{U}(s,\theta,t)\mathrm{d}s\mathrm{d}\theta$$

are approximated by solving the semi-discrete formulation

$$\frac{\mathrm{d}}{\mathrm{d}t}\overline{\mathbf{U}}_{j,k}(t) = -\frac{\mathbf{H}^F_{j+\frac{1}{2},k}(t) - \mathbf{H}^F_{j-\frac{1}{2},k}(t)}{\Delta s} - \frac{\mathbf{H}^G_{j,k+\frac{1}{2}}(t) - \mathbf{H}^G_{j,k-\frac{1}{2}}(t)}{\Delta\theta} + \overline{\mathbf{S}}_{j,k}(t), \tag{32}$$

with numerical fluxes $\mathbf{H}^F$ and $\mathbf{H}^G$ given by [25],

$$\begin{aligned}\mathbf{H}^F_{j+\frac{1}{2},k}(t) &= \frac{a^+_{j+\frac{1}{2},k}F\Big(\mathbf{U}^-_{j+\frac{1}{2},k}\Big) - a^-_{j+\frac{1}{2},k}F\Big(\mathbf{U}^+_{j+\frac{1}{2},k}\Big)}{a^+_{j+\frac{1}{2},k} - a^-_{j+\frac{1}{2},k}} \\ &\quad + \frac{a^+_{j+\frac{1}{2},k}a^-_{j+\frac{1}{2},k}}{a^+_{j+\frac{1}{2},k} - a^-_{j+\frac{1}{2},k}}\Big[\mathbf{U}^+_{j+\frac{1}{2},k} - \mathbf{U}^-_{j+\frac{1}{2},k}\Big], \\ \mathbf{H}^G_{j,k+\frac{1}{2}}(t) &= \frac{b^+_{j,k+\frac{1}{2}}G\Big(\mathbf{U}^-_{j,k+\frac{1}{2}}\Big) - b^-_{j,k+\frac{1}{2}}G\Big(\mathbf{U}^+_{j,k+\frac{1}{2}}\Big)}{b^+_{j,k+\frac{1}{2}} - b^-_{j,k+\frac{1}{2}}} \\ &\quad + \frac{b^+_{j,k+\frac{1}{2}}b^-_{j,k+\frac{1}{2}}}{b^+_{j,k+\frac{1}{2}} - b^-_{j,k+\frac{1}{2}}}\Big[\mathbf{U}^+_{j,k+\frac{1}{2}} - \mathbf{U}^-_{j,k+\frac{1}{2}}\Big].\end{aligned} \tag{33}$$

For any quantity of interest $q = q(\mathbf{U})$, the corresponding interface values are obtained via the following piece-wise linear reconstruction

$$\begin{aligned}q^-_{j+\frac{1}{2},k} &= \overline{q}_{j,k} + \frac{\Delta s}{2}(q_s)_{j,k}, \\ q^+_{j-\frac{1}{2},k} &= \overline{q}_{j,k} - \frac{\Delta s}{2}(q_s)_{j,k}, \\ q^-_{j,k+\frac{1}{2}} &= \overline{q}_{j,k} + \frac{\Delta \theta}{2}(q_\theta)_{j,k}, \\ q^+_{j,k-\frac{1}{2}} &= \overline{q}_{j,k} - \frac{\Delta \theta}{2}(q_\theta)_{j,k},\end{aligned} \tag{34}$$

where the slopes $(q_s)_{j,k}$ and $(q_\theta)_{j,k}$ are calculated using the generalized minmod limiter

$$(q_s)_{j,k} = \text{minmod}\left(\phi\frac{\overline{q}_{j,k} - \overline{q}_{j-1,k}}{\Delta s}, \frac{\overline{q}_{j+1,k} - \overline{q}_{j-1,k}}{2\Delta s}, \phi\frac{\overline{q}_{j+1,k} - \overline{q}_{j,k}}{\Delta s}\right), \tag{35}$$

$$(q_\theta)_{j,k} = \text{minmod}\left(\phi\frac{\overline{q}_{j,k} - \overline{q}_{j,k-1}}{\Delta \theta}, \frac{\overline{q}_{j,k+1} - \overline{q}_{j,k-1}}{2\Delta \theta}, \phi\frac{\overline{q}_{j,k+1} - \overline{q}_{j,k}}{\Delta \theta}\right), \tag{36}$$

where

$$\text{minmod}(z_1, z_2, \ldots) = \begin{cases} \min_j\{z_j\} & \text{if } \ z_j > 0 \ \forall j, \\ \max_j\{z_j\} & \text{if } \ z_j < 0 \ \forall j, \\ 0 & \text{otherwise.}\end{cases}$$

Here, the parameter ϕ is used to control the amount of numerical viscosity present in the resulting scheme.

The discretization of the averaged source terms

$$\overline{\mathbf{S}}_{j,k}(t) = \frac{1}{\Delta s \Delta \theta}\int_{\mathcal{C}_{j,k}}\int S(\mathbf{U})(s,\theta,t)\mathrm{d}s\mathrm{d}\theta$$

is carried out so as to satisfy the well-balanced property. This is explained in more detail in Section 4.1.

The one-sided local speeds in the s- and θ-directions, $a^\pm_{j+\frac{1}{2},k}$ and $b^\pm_{j,k+\frac{1}{2}}$, are obtained from the largest and the smallest eigenvalues of the Jacobians $\frac{\partial F(\mathbf{U})}{\partial \mathbf{U}}$ and $\frac{\partial G(\mathbf{U})}{\partial \mathbf{U}}$, respectively. Using (22) and (23), it follows that:

$$a^+_{j+\frac{1}{2},k} = \max\Big\{(\lambda^s_o)^-_{j+\frac{1}{2},k}, (\lambda^s_+)^-_{j+\frac{1}{2},k}, u^-_{j+\frac{1}{2},k}, (\lambda^s_o)^+_{j+\frac{1}{2},k}, (\lambda^s_+)^+_{j+\frac{1}{2},k}, u^+_{j+\frac{1}{2},k}, 0\Big\}, \tag{37a}$$

$$a^-_{j+\frac{1}{2},k} = \min\Big\{(\lambda^s_o)^-_{j+\frac{1}{2},k}, (\lambda^s_-)^-_{j+\frac{1}{2},k}, u^-_{j+\frac{1}{2},k}, (\lambda^s_o)^+_{j+\frac{1}{2},k}, (\lambda^s_-)^+_{j+\frac{1}{2},k}, u^+_{j+\frac{1}{2},k}, 0\Big\}, \tag{37b}$$

$$b^+_{j,k+\frac{1}{2}} = \max\Big\{(\lambda^\theta_o)^-_{j,k+\frac{1}{2}}, (\lambda^\theta_+)^-_{j,k+\frac{1}{2}}, \omega^-_{j,k+\frac{1}{2}}, (\lambda^\theta_o)^+_{j,k+\frac{1}{2}}, (\lambda^\theta_+)^+_{j,k+\frac{1}{2}}, \omega^+_{j,k+\frac{1}{2}}, 0\Big\}, \tag{37c}$$

$$b^-_{j,k+\frac{1}{2}} = \min\Big\{(\lambda^\theta_o)^-_{j,k+\frac{1}{2}}, (\lambda^\theta_-)^-_{j,k+\frac{1}{2}}, \omega^-_{j,k+\frac{1}{2}}, (\lambda^\theta_o)^+_{j,k+\frac{1}{2}}, (\lambda^\theta_-)^+_{j,k+\frac{1}{2}}, \omega^+_{j,k+\frac{1}{2}}, 0\Big\}. \tag{37d}$$

The time integration of the ODE system (32) is done using the second-order strong stability preserving Runge–Kutta scheme [15]

$$\mathbf{U}^{(1)} = \overline{\mathbf{U}}(t) + \Delta t\, \mathbf{C}[\overline{\mathbf{U}}(t)], \tag{38a}$$

$$\mathbf{U}^{(2)} = \frac{1}{2}\overline{\mathbf{U}} + \frac{1}{2}\Big(\mathbf{U}^{(1)} + \Delta t\, \mathbf{C}\Big[\mathbf{U}^{(1)}\Big]\Big), \tag{38b}$$

$$\overline{\mathbf{U}}(t+\Delta t) := \mathbf{U}^{(2)}, \tag{38c}$$

with

$$\mathbf{C}[\mathbf{U}(t)]_{j,k} = -\frac{\mathbf{H}^F_{j+\frac{1}{2},k}(t) - \mathbf{H}^F_{j-\frac{1}{2},k}(t)}{\Delta s} - \frac{\mathbf{H}^G_{j,k+\frac{1}{2}}(t) - \mathbf{H}^G_{j,k-\frac{1}{2}}(t)}{\Delta\theta} + \overline{\mathbf{S}}_{j,k}(t).$$

The Courant–Friedrichs–Lewy (CFL) condition that determines the time step Δt is

$$\Delta t \le \frac{1}{4}\min\left\{\frac{\Delta s}{a}, \frac{\Delta\theta}{b}\right\}, \tag{39}$$

where

$$a = \max_{j,k}\Big\{\max\Big(a^+_{j+\frac{1}{2},k}, -a^-_{j+\frac{1}{2},k}\Big)\Big\}, \text{ and } b = \max_{j,k}\Big\{\max\Big(b^+_{j,k+\frac{1}{2}}, -b^-_{j,k+\frac{1}{2}}\Big)\Big\}.$$

We note that a factor of $\frac{1}{4}$ is used in the CFL condition in order to guarantee the positivity-preserving property instead of the usual factor of $\frac{1}{2}$ that could be used when positivity is not an issue. A similar restriction is found in [24]. We also note that by construction, the numerical scheme is second-order in space and time in smooth regions.

4.1. Steady states at rest and positivity of the cross-sectional radius

The quantities of interest to compute the numerical flux in equation (33) are reconstructed at the interfaces via equation (34) using the minmod limiter given by equation (35). However, the reconstructed values need to be implemented carefully in order to guarantee the well-balance property. For that end, we assume that the radius at rest $R_o(s,\theta)$ is defined at the interfaces $\Big(s_j, \theta_{k\pm\frac{1}{2}}\Big)$ and at $\Big(s_{j\pm\frac{1}{2}}, \theta_k\Big)$, and we define it at the center of each cell as

$$R_{o,j,k} := \frac{1}{4}\Big[R_o\Big(s_{j-\frac{1}{2}}, \theta_k\Big) + R_o\Big(s_{j+\frac{1}{2}}, \theta_k\Big) + R_o\Big(s_j, \theta_{k-\frac{1}{2}}\Big) + R_o\Big(s_j, \theta_{k+\frac{1}{2}}\Big)\Big]. \tag{40}$$

On the other hand, the angle $\alpha(s)$ is defined at each interface point $s_{j+\frac{1}{2}}$. The derivatives both at the center of each cell and at the interfaces are approximated via centered differences as

$$\alpha(s_j) \approx \frac{\alpha\Big(s_{j+\frac{1}{2}}\Big) + \alpha\Big(s_{j-\frac{1}{2}}\Big)}{2}, \quad \alpha'(s_j) \approx \frac{\alpha\Big(s_{j+\frac{1}{2}}\Big) - \alpha\Big(s_{j-\frac{1}{2}}\Big)}{\Delta s}, \quad \alpha'\Big(s_{j+\frac{1}{2}}\Big) \approx \frac{\alpha(s_{j+1}) - \alpha(s_j)}{\Delta s} \tag{41}$$

which gives

$$A_{o,j+\frac{1}{2},k} = \frac{R^2_{o,j+\frac{1}{2},k}}{2} - \frac{R^3_{o,j+\frac{1}{2},k}}{3}\sin(\theta_k)\alpha'\Big(s_{j+\frac{1}{2}}\Big),$$

$$A_{o,j,k+\frac{1}{2}} = \frac{R^2_{o,j,k+\frac{1}{2}}}{2} - \frac{R^3_{o,j,k+\frac{1}{2}}}{3}\sin\Big(\theta_{k+\frac{1}{2}}\Big)\alpha'(s_j).$$

In order to reconstruct A at the interfaces, we define $\mathcal{A} = A/A_o$ and reconstruct the values $\mathcal{A}^{\pm}_{j+\frac{1}{2},k}$ and $\mathcal{A}^{\pm}_{j,k+\frac{1}{2}}$ at the cell interfaces using equation (34). The cross-sectional area at the cell interfaces are then given by

$$A^{\pm}_{j+\frac{1}{2},k} = \mathcal{A}^{\pm}_{j+\frac{1}{2},k}A_{o,j+\frac{1}{2},k}, \quad A^{\pm}_{j,k+\frac{1}{2}} = \mathcal{A}^{\pm}_{j,k+\frac{1}{2}}A_{o,j,k+\frac{1}{2}}. \tag{42}$$

This way, if $R = R_o$ or equivalently $A = A_o$ at the center of each cell (as it occurs for steady states at rest), the same equality holds at the cell interfaces. Once the variable A is reconstructed, this gives the reconstruction for R by inverting it in terms of A. One also obtains the reconstruction for the parameter Γ via the relation

$$\Gamma^{\pm}_{j+\frac{1}{2},k} = R^{\pm}_{j+\frac{1}{2},k}\sin(\theta_k)^{\pm}\alpha'\Big(s_{j+\frac{1}{2}}\Big), \quad \Gamma^{\pm}_{j,k+\frac{1}{2}} = R^{\pm}_{j,k+\frac{1}{2}}\sin\Big(\theta_{k+\frac{1}{2}}\Big)\alpha'(s_j). \tag{43}$$

This immediately defines all the parameter functions $\psi_{s,o}$, $\psi_{s,1}$, $\psi_{s,2}$, $\psi_{\theta,1}$, $\psi_{\theta,2}$ and A_θ at the interfaces. The conserved variables $Q_1 = \psi_{s,o}Au$ and $Q_2 = AL$ are reconstructed directly via equation (34), from which we can recover the reconstructed values for $u = \frac{Q_1}{\psi_{s,o}A}$, $L = \frac{Q_2}{A}$, and $\omega = \frac{L}{A_\theta}$.

The source terms in equation (17) do not involve derivatives of the solution itself and one can use the cell averages to discretize them. The partial derivatives $\partial_2\bar{p}$ and $\partial_3\bar{p}$ are with respect to the explicit dependance of the fixed parameters involved in the definition of the transmural pressure. For instance, the transmural pressure p given by equation (28) involves the radius at rest $R_o(s,\theta)$ and the parameter $G_o(s,\theta)$. The parameter $G_o(s,\theta)$ is defined at the interfaces $\Big(s_j, \theta_{k\pm\frac{1}{2}}\Big)$ and $\Big(s_{j\pm\frac{1}{2}}, \theta_k\Big)$, and we define it at the center of each cell as

$$G_{o,j,k} := \frac{1}{4}\Big[G_o\Big(s_{j-\frac{1}{2}},\theta_k\Big) + G_o\Big(s_{j+\frac{1}{2}},\theta_k\Big) + G_o\Big(s_j,\theta_{k-\frac{1}{2}}\Big) + G_o\Big(s_j,\theta_{k+\frac{1}{2}}\Big)\Big]. \tag{44}$$

The terms $\partial_2\bar{p}$ and $\partial_3\bar{p}$ are given explicitly by equation (30). In that case, one only needs partial derivatives of G_o and A_o which are approximated as

$$\begin{aligned}
\partial_2 G_o(s_j,\theta_k) &\approx \frac{G_o\Big(s_{j+\frac{1}{2},k}\Big) - G_o\Big(s_{j-\frac{1}{2},k}\Big)}{\Delta s},\\
\partial_3 G_o(s_j,\theta_k) &\approx \frac{G_o\Big(s_{j,k+\frac{1}{2}}\Big) - G_o\Big(s_{j,k-\frac{1}{2}}\Big)}{\Delta\theta},
\end{aligned} \tag{45}$$

$$\begin{aligned}
\partial_2 A_o(s_j,\theta_k) &\approx \frac{A_o\Big(s_{j+\frac{1}{2},k}\Big) - A_o\Big(s_{j-\frac{1}{2},k}\Big)}{\Delta s},\\
\partial_3 A_o(s_j,\theta_k) &\approx \frac{A_o\Big(s_{j,k+\frac{1}{2}}\Big) - A_o\Big(s_{j,k-\frac{1}{2}}\Big)}{\Delta\theta}.
\end{aligned} \tag{46}$$

In a steady state at rest given by equation (31), the reconstructed values of u and ω are zero, and the equality $R = R_o$ holds at the interfaces. As a result, all the numerical fluxes $\mathbf{H}^F_{j+\frac{1}{2},k}, \mathbf{H}^G_{j,k+\frac{1}{2}}$ and the source terms $\overline{\mathbf{S}}_{j,k}$ vanish. We have proved the following proposition.

Proposition 2. *Consider system (15)–(17) with transmural pressure given by (28). Then, the numerical scheme (33)–(39) with the discretizations given by (40)–(46) is well-balanced, i.e., $\overline{\mathbf{U}}(t+\Delta t) = \overline{\mathbf{U}}(t)$ for steady states at rest.*

The following proposition shows that the CFL condition (39) guarantees the positivity of A when the solution is computed with the Runge–Kutta method (38) and a slight modification is applied to the reconstruction at the interfaces. This is particularly important in situations where the cross section is small. This is not a relevant case from the medical point of view. However, we present it here for the sake of completeness and it would be useful for applications involving collapsed tubes.

Since we have reconstructed $\mathcal{A} = A/A_o$ at the interfaces,

$$\overline{A}_{j,k} = \frac{1}{4}\Big[A^{+}_{j-\frac{1}{2},k} + A^{-}_{j+\frac{1}{2},k} + A^{-}_{j,k+\frac{1}{2}} + A^{+}_{j,k-\frac{1}{2}}\Big] \tag{47}$$

does not necessarily hold unless A_o is constant. In the cases where one decides to implement the positivity-preserving property, a modification in the reconstruction must be implemented. Namely,

$$\mathcal{A}^{-}_{j+\frac{1}{2},k} = \overline{\mathcal{A}}_{j,k} + \frac{\Delta s}{2}(\mathcal{A}_s)_{j,k} \tag{48a}$$

$$A^{-}_{j+\frac{1}{2},k} = \min\Big(\max\Big\{\mathcal{A}^{-}_{j+\frac{1}{2},k}A_{o,j+\frac{1}{2},k}, A_{th}\Big\}, 2\bar{A}_{j,k}\Big) \tag{48b}$$

$$A^{+}_{j-\frac{1}{2},k} = 2\bar{A}_{j,k} - A^{-}_{j+\frac{1}{2},k} \tag{48c}$$

with the analogous procedure for $A^{\pm}_{j,k\pm\frac{1}{2}}$. Here A_{th} is a threshold value needed to maintain positivity in the reconstruction of the interface values. The threshold value can be chosen empirically. This has been done in different contexts and it has shown to be useful in achieving the positivity-preserving property. See for instance [23], where a scheme with this property was derived for the shallow water equations. The threshold will be used only when the corresponding variable (cross sectional area in our case) is small and there is a risk of getting negative unphysical values. Despite the fact that the threshold is obtained empirically, it does not affect the performance of the numerical scheme and the alternative of not using it could result in unphysical situations. In this work, we did not include numerical tests where a threshold is needed but it could be used in a future work.

Equation (48b) guarantees that $0 \le A^{-}_{j+\frac{1}{2},k} \le 2\bar{A}_{j,k}$, and the discretization is consistent with the equations. Equation (48c) guarantees $A^{+}_{j-\frac{1}{2},k} \ge 0$. As a result, the above corrections ensure the positivity of the reconstructed values as well as the relation in equation (47) needed in the proof below. It is also important to mention that the above corrections does not affect the well-balance property.

Proposition 3. *Consider the scheme with the reconstruction algorithm described in Section 4.1. If the cell averages $\overline{A}_{j,k}(t)$ are such that*

$$\overline{A}_{j,k}(t) \ge 0 \quad \forall\, j,k$$

then the cell averages $\overline{A}_{j,k}(t+\Delta t)$ computed with the Runge–Kutta method (38) for all j,k, under the CFL limitation (39), will yield

$$\overline{A}_{j,k}(t+\Delta t) \ge 0 \quad \forall\ j,k.$$

Proof. Since our Runge–Kutta numerical scheme can be written as a convex combination of Euler steps, one only needs to prove it for just one forward Euler step. The first component in equation (32) can be written as

$$\begin{aligned}\overline{A}_{j,k}(t+\Delta t) = \overline{A}_{j,k}(t) &- \frac{\Delta t}{\Delta s}\left[\left(\mathbf{H}^{F}_{j+\frac{1}{2},k}\right)^{(1)} - \left(\mathbf{H}^{F}_{j-\frac{1}{2},k}\right)^{(1)}\right] \\ &- \frac{\Delta t}{\Delta \theta}\left[\left(\mathbf{H}^{G}_{j,k+\frac{1}{2}}\right)^{(1)} - \left(\mathbf{H}^{G}_{j,k-\frac{1}{2}}\right)^{(1)}\right].\end{aligned}$$

Using (33), we can rewrite it as

$$\overline{A}_{j,k}(t+\Delta t) = \left[\frac{1}{4} - \frac{\Delta t}{\Delta s}a^{+}_{j+\frac{1}{2},k}\frac{u^{-}_{j+\frac{1}{2},k} - a^{-}_{j+\frac{1}{2},k}}{a^{+}_{j+\frac{1}{2},k} - a^{-}_{j+\frac{1}{2},k}}\right]A^{-}_{j+\frac{1}{2},k} + \left[\frac{1}{4} + \frac{\Delta t}{\Delta s}a^{-}_{j-\frac{1}{2},k}\frac{a^{+}_{j-\frac{1}{2},k} - u^{+}_{j-\frac{1}{2},k}}{a^{+}_{j-\frac{1}{2},k} - a^{-}_{j-\frac{1}{2},k}}\right]A^{+}_{j-\frac{1}{2},k}$$

$$
\begin{aligned}
&+\left[\frac{1}{4}-\frac{\Delta t}{\Delta\theta}b^{+}_{j,k+\frac{1}{2}}\frac{\omega^{-}_{j,k+\frac{1}{2}}-b^{-}_{j,k+\frac{1}{2}}}{b^{+}_{j,k+\frac{1}{2}}-b^{-}_{j,k+\frac{1}{2}}}\right]A^{-}_{j,k+\frac{1}{2}}+\left[\frac{1}{4}+\frac{\Delta t}{\Delta\theta}b^{-}_{j,k-\frac{1}{2}}\frac{b^{+}_{j,k-\frac{1}{2}}-\omega^{+}_{j,k-\frac{1}{2}}}{b^{+}_{j,k-\frac{1}{2}}-b^{-}_{j,k-\frac{1}{2}}}\right]A^{+}_{j,k-\frac{1}{2}}\\
&-\frac{\Delta t}{\Delta s}a^{-}_{j+\frac{1}{2},k}\frac{a^{+}_{j+\frac{1}{2},k}-u^{+}_{j+\frac{1}{2},k}}{a^{+}_{j+\frac{1}{2},k}-a^{-}_{j+\frac{1}{2},k}}A^{+}_{j+\frac{1}{2},k}+\frac{\Delta t}{\Delta s}a^{+}_{j-\frac{1}{2},k}\frac{u^{-}_{j-\frac{1}{2},k}-a^{-}_{j-\frac{1}{2},k}}{a^{+}_{j-\frac{1}{2},k}-a^{-}_{j-\frac{1}{2},k}}A^{-}_{j-\frac{1}{2},k}\\
&-\frac{\Delta t}{\Delta\theta}b^{-}_{j,k+\frac{1}{2}}\frac{b^{+}_{j,k+\frac{1}{2}}-\omega^{+}_{j,k+\frac{1}{2}}}{b^{+}_{j,k+\frac{1}{2}}-b^{-}_{j,k+\frac{1}{2}}}A^{+}_{j,k+\frac{1}{2}}+\frac{\Delta t}{\Delta\theta}b^{+}_{j,k-\frac{1}{2}}\frac{\omega^{-}_{j,k-\frac{1}{2}}-b^{-}_{j,k-\frac{1}{2}}}{b^{+}_{j,k-\frac{1}{2}}-b^{-}_{j,k-\frac{1}{2}}}A^{-}_{j,k-\frac{1}{2}}\\
&+\overline{A}_{j,k}-\frac{1}{4}\Big[A^{+}_{j-\frac{1}{2},k}+A^{-}_{j+\frac{1}{2},k}+A^{-}_{j,k+\frac{1}{2}}+A^{+}_{j,k-\frac{1}{2}}\Big].
\end{aligned}
$$

The first four terms in the above equation will be non negative under the CFL restriction (39). Also, since $a^{-}_{j+\frac{1}{2},k}\leq 0$, $b^{-}_{j,k+\frac{1}{2}}\leq 0$, $a^{+}_{j-\frac{1}{2},k}\geq 0$ and $b^{+}_{j,k-\frac{1}{2}}\geq 0$, the following four terms in the above equation are also non negative, which concludes the proof. □

5. Numerical experiments

Different numerical experiments are presented to show the merits of the numerical scheme and the dynamics of the flow given by the model derived in this paper. One can analyze situations where vessels exhibit non-uniform elasticity properties and the effect on the dynamics of the flow. In the following tests, we focus on the variations of velocity, pressure and wall's deformation in the angular directions, which is indeed easily captured by the proposed 2D model. It can occur for instance, in vessels with damaged regions leading to asymmetric elasticity properties. The axial velocity at damaged regions is analyzed is numerical examples 5.3 and 5.4. In example 5.3, this velocity is compared between a non-damaged vessel and a damaged vessel (similar to an idealized aneurysma) with a localized damaged area.

The velocity field in 3D views of the artery is computed as follows. First, we need to compute the curvature radius, which is given by

$$
R_c=\frac{\left(R^2+R_\theta^2\right)^{\frac{3}{2}}}{R^2+2R_\theta^2-RR_{\theta\theta}}=\frac{R\Big(1+\big(\frac{R_\theta}{R}\big)^2\Big)^{\frac{3}{2}}}{1+2\big(\frac{R_\theta}{R}\big)^2-\frac{R_{\theta\theta}}{R}},
$$

where

$$
R_\theta=\partial_\theta R,\quad R_{\theta\theta}=\partial^2_{\theta\theta}R.
$$

The total velocity at each point

$$
(x(s,\theta),y(s,\theta),z(s,\theta))=(-R\sin(\alpha(s))\sin(\theta)+x_o(s),R\cos(\theta),R\cos(\alpha(s))\sin(\theta)+z_o(s))
$$

is given by

$$
\mathbf{V}(s,\theta)=\begin{pmatrix}\cos(\alpha(s))\\0\\\sin(\alpha(s))\end{pmatrix}u+\frac{\frac{R_c}{R}}{\Big(1+\big(\frac{R_\theta}{R}\big)^2\Big)^{\frac{1}{2}}}\begin{pmatrix}-\sin(\alpha(s))\Big(\cos(\theta)+\frac{R_\theta}{R}\sin(\theta)\Big)\\-\sin(\theta)+\frac{R_\theta}{R}\cos(\theta)\\\cos(\alpha(s))\Big(\cos(\theta)+\frac{R_\theta}{R}\sin(\theta)\Big)\end{pmatrix}U_{Tang},\tag{49}
$$

where

$$
U_{Tang}=\frac{1}{A}\int_o^R rV_\theta|J|\mathrm{d}r.\tag{50}
$$

For convenience and ease of notation, we define $\mathcal{R} = R/R_o$ at the center of each cell.

In all cases, we apply periodic boundary conditions in θ. The boundary conditions in the axial directions are specified in each numerical test. Also, the parameters used for these numerical experiments are as follows. The blood density is $\rho = 1050$ kg m^{-3}, blood viscosity coefficient $\nu = 4$ cP, $\beta = 2$, $\gamma_s = 9$, $\gamma_\theta = 2$, Young's modulus $E_Y = 400$ kPa and $h_d = 0.5$ mm. Finally, we take $r_d = R_o$.

5.1. Horizontal vessel with tapering: evolution of perturbation

In this first numerical test, we consider the simple case of a horizontal vessel ($\alpha(s) = 0$) with tapering. That is, A_o is given by

$$A_o(s,\theta) = A_o^\star(1 - sT_p), \quad R_o(s,\theta) = \sqrt{2A_o(s,\theta)},$$

where $T_p = 0.005$ cm^{-1} is the tapering factor and $A_o^\star = (0.82\text{ cm})^2$. The initial vessel's radius consists of a perturbation from a steady state. The perturbation is located in the middle of the artery. Specifically, the center is at $s^\star = 25$ cm and $\theta^\star = \frac{\pi}{4}$ rad. The initial radius is then given by

$$R(0,s,\theta) = \mathcal{R}(0,s,\theta)R_o(s,\theta), \text{ where}$$

$$\mathcal{R}(0,s,\theta) = \begin{cases} 1 & \text{if } \frac{d(s,\theta)}{R_o(s^\star,\theta^\star)} > 1, \\ 1 + \frac{1}{5}\sin\left(\left[1 - \frac{d(s,\theta)}{R_o(s^\star,\theta^\star)}\right]\frac{\pi}{2}\right) & \text{if } \frac{d(s,\theta)}{R_o(s^\star,\theta^\star)} \le 1 \end{cases}$$

and

$$d(s,\theta) = \sqrt{\frac{1}{4}[x(s^\star,\theta^\star) - x(s,\theta)]^2 + [y(s^\star,\theta^\star) - y(s,\theta)]^2 + [z(s^\star,\theta^\star) - z(s,\theta)]^2}.$$

Neumann boundary conditions are imposed at both ends ($s = 0,\ s_L$) with $s_L = 50$ cm.

In this first numerical test, the initial conditions consist of a radius perturbation from a steady state. That is, the transmural pressure is zero everywhere in the artery, except in an area near $(s^\star, \theta^\star)$ where the radius is above the steady state one and the transmural pressure becomes positive. Figure 2 shows a 3D view of the artery with the above initial conditions in panel (a). This generates a displacement that consists of a radial expansion at early times, and it can be observed in panels (b) and (c). The color bar indicates the ratio of the vessel radius at time t and its initial value ($R(t;s,\theta)/R_o(s,\theta)$), which can help us identify the evolution of the perturbation. The initial perturbation covers only a partial side of the artery's wall and the displacement goes in both the axial and angular directions. At later times in panels (d) and (e), the displacement has already reached the opposite side of the wall and it has come back to the initial location by periodicity in the angular direction. The last panel (f) shows the solution at time $t = 0.1$ s where the displacement has already propagated in the axial direction outside the visualized region. As a result, the artery has recovered its initial unperturbed steady state.

5.2. Aorta vessel with discharge

The previous case showed that the model and the numerical scheme produces good results for perturbations to steady states in horizontal vessels. For the rest of the numerical tests, we will consider geometries similar to an idealized aorta without branches.

Let $R_o^\star(s)$ be the piecewise linear function of s obtained according to the radius at diastolic pressure shown in [40, Table IV], which we present in Table 1 for the convenience of the reader. The initial conditions for the artery's geometry is described by cross sections given by

$$R_o(s,\theta) = R_o^\star(s)h(\theta),$$

where $h(\theta)$ is a function that determines the type of cross section that we may have. We note that we obtain circular cross sections when $h(\theta)$ is constant. As it is reported in [26], however, we may observe cross sections

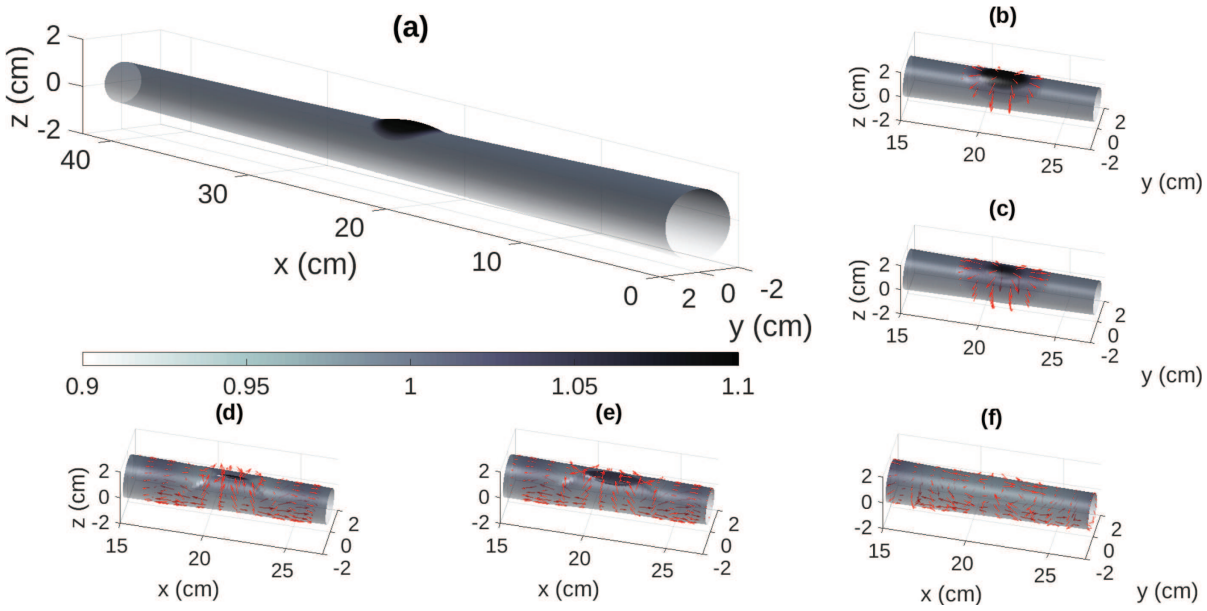

FIGURE 2. A 3D view of the vessel. The arrows near the wall indicate the velocity field given by equation (49). The color bar indicates the ratio of the vessel radius at time t and the unstressed value $(R(t;s,\theta)/R_o(s,\theta))$. The initial conditions, which consists of a radius perturbation near $s^\star = 25$ cm and $\theta^\star = \pi/4$ rad is shown in (a), where the entire artery is visualized. The rest of the panels show a section 15 cm $\leq s \leq$ 35 cm where the perturbation evolves at times $t = 0.0005$ s (b), $t = 0.001$ s (c), $t = 0.0045$ s (d), $t = 0.005$ s (e) and $t = 0.1$ s (f). The arrows indicate the 3D velocity field given by equation (49).

TABLE 1. Description of aorta's geometry and dimensions. The segments, their lengths, left and right radii are shown in the first four columns. Such values were obtained from [40, Table IV].

Segment	Length (cm)	Left radius (cm)	Right radius (cm)
I	7.0357	1.52	1.39
II	0.8	1.39	1.37
III	0.9	1.37	1.35
IV	6.4737	1.35	1.23
V	15.2	1.23	0.99
VI	1.8	0.99	0.97
VII	0.7	0.97	0.962
VIII	0.7	0.962	0.955
IX	4.3	0.955	0.907
X	4.3	0.907	0.86

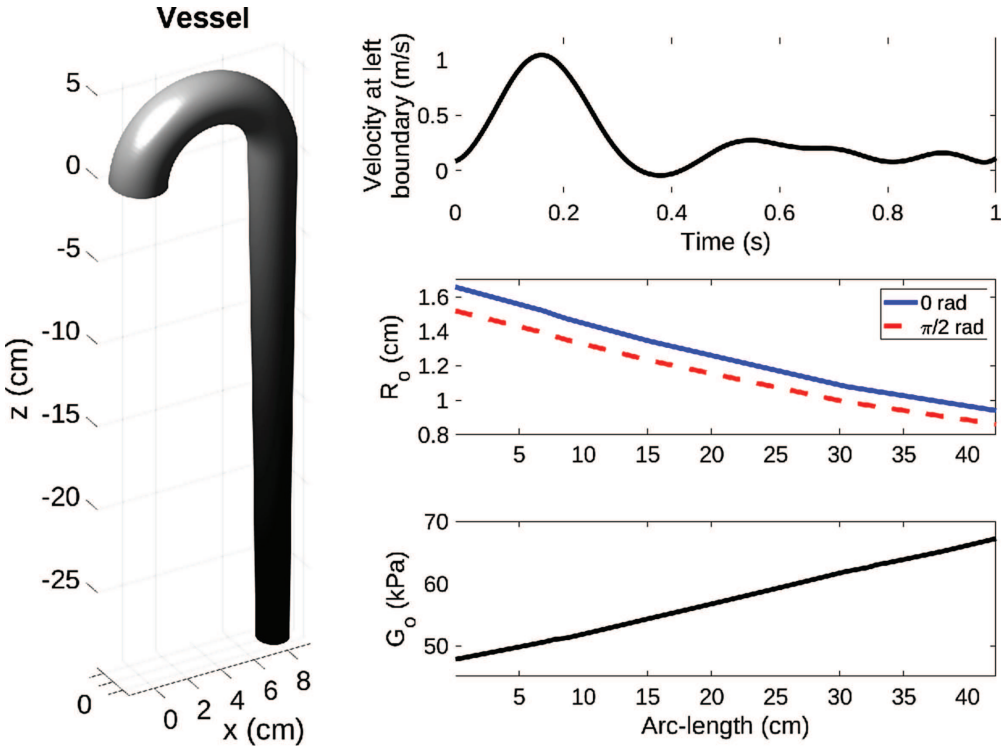

FIGURE 3. Blood flow simulation passing through the full aorta. Left panel: 3D view of the aorta. Top right: Velocity at the left boundary in a cardiac cycle as a function of time. Middle right: Profile of R_o as a function of arc-length s for different angles. Bottom right: Profile of G_o as function of arc-length s.

that have an elliptical-like shape in the aorta. We then choose

$$h(\theta) = \sqrt{\frac{1-\xi^2 \sin(\theta)^2}{1-\xi^2}},$$

where ξ is the eccentricity and $\xi \in [0,1)$. Graphs of R_o as a function of axial position s for different values of θ are displayed in the middle right panel of Figure 3 .

The parameter $G_o^\star(s)$ is given by equation (29). A graph of G_o is displayed in the bottom right panel of Figure 3. As an approximation to the aorta's curvature, the angle $\alpha(s)$ is given by

$$\alpha(s) = \begin{cases} \left[1 - \frac{s}{12.63 \text{ cm}}\right]\frac{\pi}{2} & \text{if } 0 \le s \le 12.63 \text{ cm}, \\ -\frac{\pi}{2} & \text{if } s > 12.63 \text{ cm}. \end{cases}$$

That is, the vessel is straight up at the upstream boundary $\alpha(0 \text{ cm}) = \pi/2$ and points down at $s = 12.63$ cm, where $\alpha(12.63 \text{ cm}) = -\pi/2$. Figure 3 (left panel) shows a 3D view of the tapered vessel at time $t = 0$ s (seconds not to be confused with arclength's position). Here, we use 200 grid points in the axial direction and 180 grid points in the angular direction. The initial condition is given by $A = A_o$, $u = 0$ and $L = 0$ in a tilted vessel with elliptical geometric shape ($\xi = 0.4$), which would have corresponded to a steady state if the vessel was horizontal.

At the left boundary ($s = 0$), we impose a velocity that corresponds to a cardiac cycle (to be specified below) and Dirichlet boundary conditions for the radius $R = R_o$ and $\omega = 0$. The discharge at the left boundary breaks

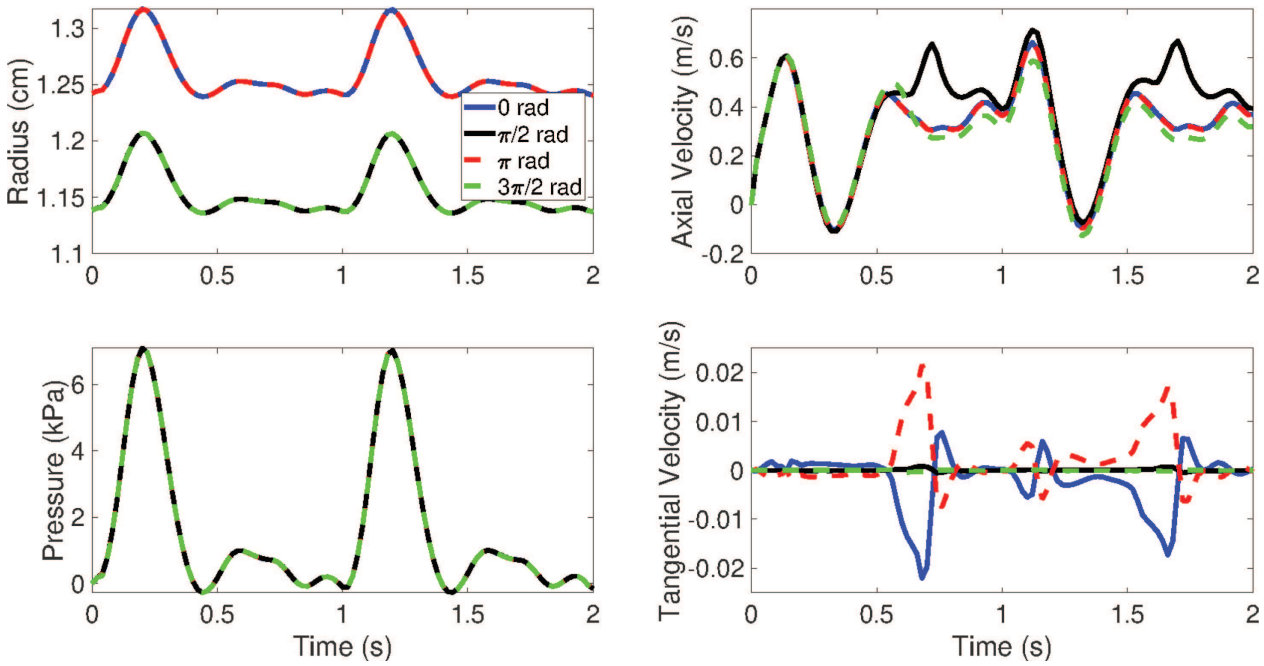

FIGURE 4. Profiles as a function of time at $s = 21.10$ cm. Top left: Radius R at different angles. Top right: Axial velocity u. Bottom left: Pressure p. Bottom right: Tangential velocity U_{Tang}.

the balance and induces a moving state. Neumann boundary conditions are imposed at the right boundary. The time series for the velocity at the left boundary was obtained from [5], and it was approximated using the first 15 elements of its Fourier decomposition. Initially, the velocity at the left boundary increases up to speeds above 1 ms^{-1}. A graph of the inlet velocity as a function of time can be found in the top right panel of Figure 3 .

In Figure 4, we show the evolution of four variables, radius R, axial velocity u, pressure p and tangential velocity U_{Tang}, over 2 seconds at $s = 21.10$ cm. Here, the vessel's radius R is increased due to the influence of the inlet velocity given by the cardiac cycle. On the hand, the transmural pressure reaches its maximum of approximately 7.1 kPa near $t = 0.2$ seconds, followed by a decay. Here, the transmural pressure profile are similar for each θ. In the top right panel we observe the evolution of the axial velocity. Since the initial condition is $u = 0$, the profile starts with an increment to 0.61 ms^{-1}, followed by a decay to -0.1 ms^{-1}, and by an increment to 0.44 ms^{-1} reached at 0.52 s. After this time, the profiles given by different θ values diverge from each other. At $\theta = \pi/2$ rad the velocity reached a maximum of approximately 0.69 ms^{-1} at $t = 0.70$ s, while the other profiles show a decay to 0.31 ms^{-1} at the same time. After that, the profiles evolve in a quasi-periodic way.

Finally, the tangential velocity profiles are shown in the bottom right panel of Figure 4. Here, we observe that the value is much lower than the axial velocity. One can observe that the tangential velocities are much weaker at angles $\theta = \pi/2$ and $\theta = 3\pi/2$ rad, while the other two ($\theta = 0$ and $\theta = \pi$ rad) are approximately opposite in sign.

5.3. Idealized aorta vessel with a bulge

Non-uniform elasticity properties in a vessel may be caused by diseases such as stenosis and aneurysms. In this numerical test, we analyze possible changes in the flow dynamics when the parameters G_o and R_o are non-uniform in a localized regions in the artery's wall. In particular, G_o is reduced at ($s = s^\star = 21$ cm, $\theta =$

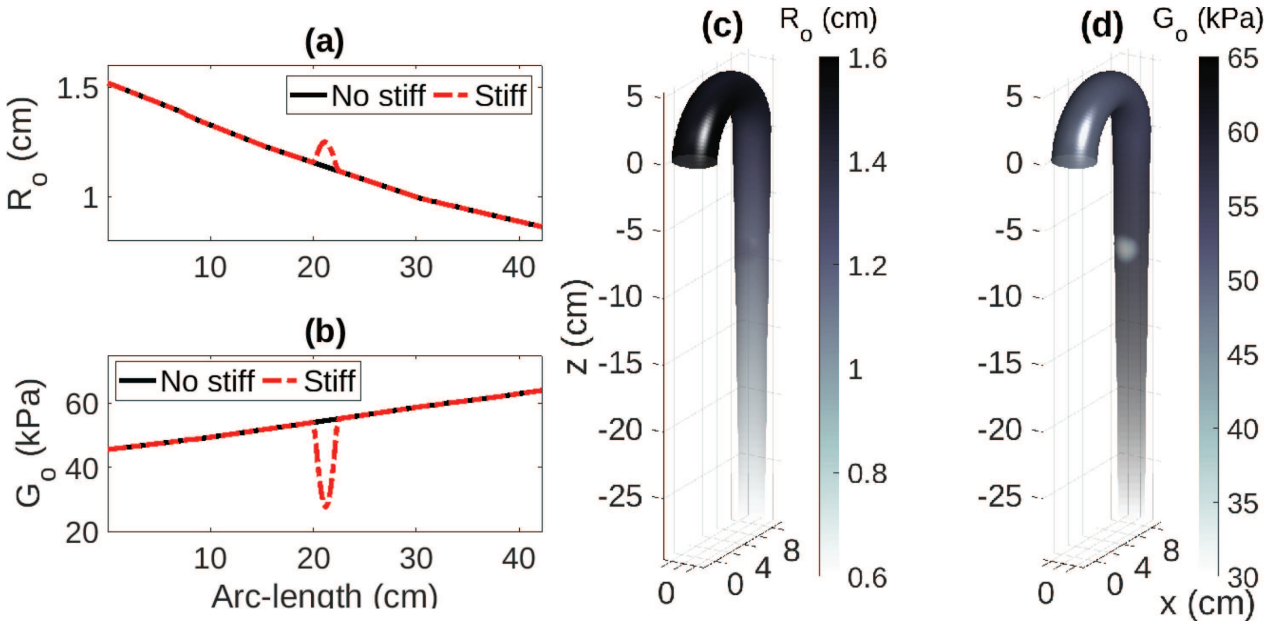

FIGURE 5. Parameters for an artery with a bulge in a localized region where the wall is less rigid. In black solid line, profiles of G_o (panel (a)) and R_o (panel (b)) at $\theta = 3\pi/2$ rad are shown, while the red dotted lines correspond to the base case with no bulging. The profiles are given by equations (51) and (52). Panel (c): 3D visualization of an idealized aorta where the color bar denotes G_o values. Panel (d): same a in middle panel with R_o values in the color bar.

$\theta^\star = 3\pi/2$) and R_o is increased near that point, when compared to the previous case. Such changes in the parameters are aimed at simulating an artery with a bulge in a localized region where the artery is also less rigid.

The parameters G_o and R_o are given by

$$G_o(s,\theta) = \begin{cases} G_o^\star(s) & \text{if } d(s,\theta) > h(\theta)R_o^\star(s), \\ \left[1 - \frac{1}{2}\sin\left(\left[1 - \frac{d(s,\theta)}{h(\theta)R_o^\star(s)}\right]\frac{\pi}{2}\right)\right]G_o^\star(s) & \text{if } d(s,\theta) \le h(\theta)R_o^\star(s), \end{cases} \tag{51}$$

and

$$R_o(s,\theta) = \begin{cases} h(\theta)R_o^\star(s) & \text{if } d(s,\theta) > h(\theta)R_o^\star(s), \\ \left[1 + \frac{1}{5}\sin\left(\left[1 - \frac{d(s,\theta)}{h(\theta)R_o^\star(s)}\right]\frac{\pi}{2}\right)\right]h(\theta)R_o^\star(s) & \text{if } d(s,\theta) \le h(\theta)R_o^\star(s), \end{cases} \tag{52}$$

where

$$d(s,\theta) = \sqrt{\frac{1}{4}\left[x(s^\star,\theta^\star) - x(s,\theta)\right]^2 + \left[y(s^\star,\theta^\star) - y(s,\theta)\right]^2 + \left[z(s^\star,\theta^\star) - z(s,\theta)\right]^2}.$$

A graph of the parameters at $\theta = 3\pi/2$ rad as a function of s is shown in panels (a) and (b) in Figure 5. A 3D visualization of the aorta using R_o (c) and G_o (d) in the color bar are displayed to localize the region where the elasticity properties of the artery vary.

As initial conditions, we set

$$R(0,s,\theta) = R_o(s,\theta), \quad u(0,s,\theta) = 0 \quad \text{and} \quad L(0,s,\theta) = 0.$$

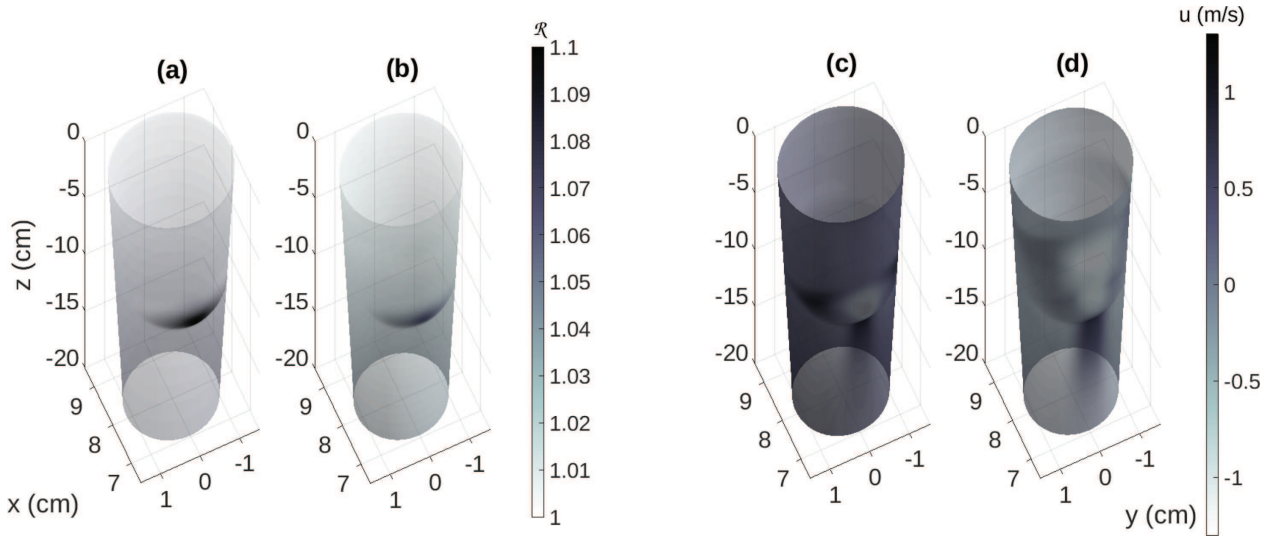

FIGURE 6. Panels (a) and (b): 3D view of the artery with color bar computed based on $\mathcal{R} = R/R_o$ at times $t = 0.2$ s and $t = 0.3$ s respectively. Panels (c) and (d): Same as in (a) and (b) with a color bar computed based on u.

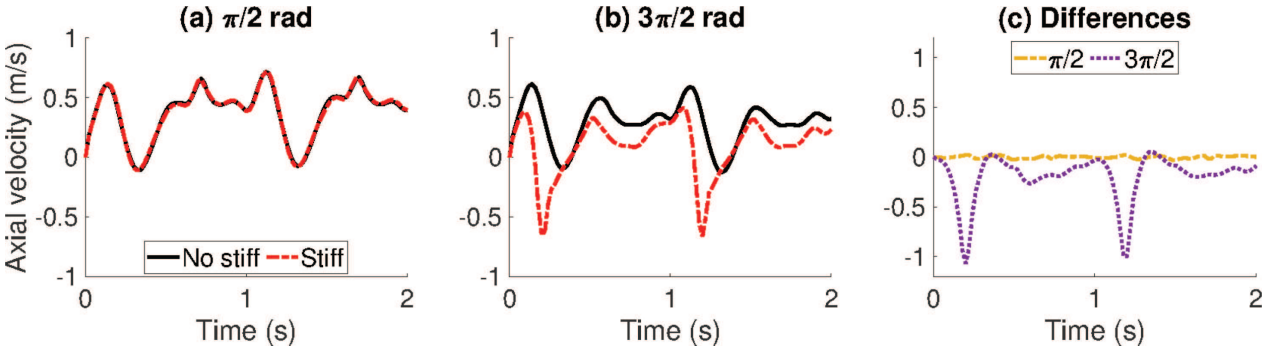

FIGURE 7. Axial velocity profiles as a function of time at $s = 21$ cm. Panel (a): Profiles at $\theta = \pi/2$ rad. Panel (b): Profiles at $\theta = 3\pi/2$ rad. Panel (c): Profile differences for $\theta = \pi/2$ rad (ocher dashed line) and $\theta = 3\pi/2$ rad (purple dotted line).

Figure 6 shows the effect of the bulge with non-uniform elasticity parameters in the flow dynamics. For instance, panels (a) and (b) show a 3D view of the artery near the bulge where the color bar indicates the ratio R/R_o at times $t = 0.2$ s and $t = 0.3$ s respectively. Such ratio indicates how much the artery's radius has been deformed from the initial conditions. One can observe a stronger deviation from the initial conditions (about 10%) near the bulge at $t = 0.2$ s, when compared to the rest of the artery. Such deviation is reduced at $t = 0.3$ s. On the other hand, a color bar computed based on the axial velocity is displayed in panels (c) and (d). We observe a negative displacement in the upper side of the bulge and a positive displacement in the lower side of the bulge at $t = 0.3$ s. However, the axial velocity becomes positive everywhere at later times (not shown) due to gravity and the fluid discharge in the upstream boundary.

Figure 7 exhibits a quantification of the observations discussed in Figure 6. Specifically, the axial velocity as a function of time at $s = s^\star$, $\theta = \pi/2$ and $\theta = 3\pi/2$ rad are displayed in panels (a) and (b) respectively. For

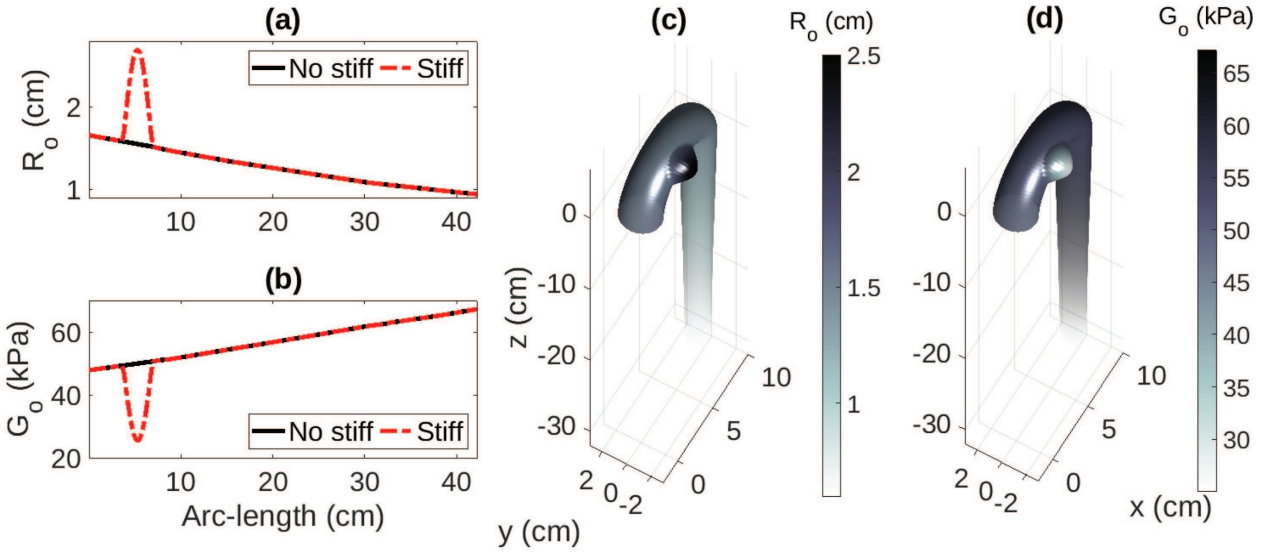

FIGURE 8. Parameters R_o and G_o given by equations (53) and (54) as a function of s at $\theta = \pi$ rad are shown in panels (a) and (b) respectively (red dotted lines). The black solid lines correspond to the base case in Section 5.2. Panel (c): 3D view with color bar denoting R_o. Panel (d): same as in (c) with G_o values in the color bar.

comparison, we include a graph corresponding to the base case in Section 5.2. The bulge is at $\theta = 3\pi/2$ rad (panel (b)), where the velocity is decreasing near it. The differences could be up to about 1 ms^{-1}, as we see it in panel (c). Panel (a) shows the axial velocities experienced by the fluid on the opposite side of the wall, where the impact of the bulge does not seem to be significant in the time window considered here.

5.4. Vortex-like structure in aorta vessel with a bulge

In this numerical example, we consider a situation where the G_o parameter has a negative perturbation in a localized lateral section of the artery near the upstream boundary and R_o is also increased in the same sector, as specified below (see Fig. 8). This situation is associated with an idealized thoracic aortic aneurysm [17], where the artery's wall is less rigid in a localized zone. The two parameters G_o and R_o are given by

$$G_o(s,\theta) = \begin{cases} G_o^\star(s) & \text{if } d(s,\theta) > h(\theta)R_o^\star(s), \\ \left[1 - \frac{1}{2}\sin\left(\left[1 - \frac{d(s,\theta)}{h(\theta)R_o^\star(s)}\right]\frac{\pi}{2}\right)\right]G_o^\star(s) & \text{if } d(s,\theta) \le h(\theta)R_o^\star(s), \end{cases} \tag{53}$$

and

$$R_o(s,\theta) = \begin{cases} h(\theta)R_o^\star(s) & \text{if } d(s,\theta) > h(\theta)R_o^\star(s), \\ \left[1 + \frac{3}{4}\sin\left(\left[1 - \frac{d(s,\theta)}{h(\theta)R_o^\star(s)}\right]\frac{\pi}{2}\right)\right]h(\theta)R_o^\star(s) & \text{if } d(s,\theta) \le h(\theta)R_o^\star(s), \end{cases} \tag{54}$$

where

$$d(s,\theta) = \sqrt{[x(s^\star,\theta^\star) - x(s,\theta)]^2 + [y(s^\star,\theta^\star) - y(s,\theta)]^2 + [z(s^\star,\theta^\star) - z(s,\theta)]^2},$$
$$s^\star = 5 \text{ cm}, \quad \theta^\star = \pi \text{ rad}.$$

A 3D view of the artery at time $t = 0.4$ s can be found in panels (a) and (b) of Figure 9, respectively. In each panel, the velocity field is shown to analyze the change in the dynamic. The color bar shows the axial

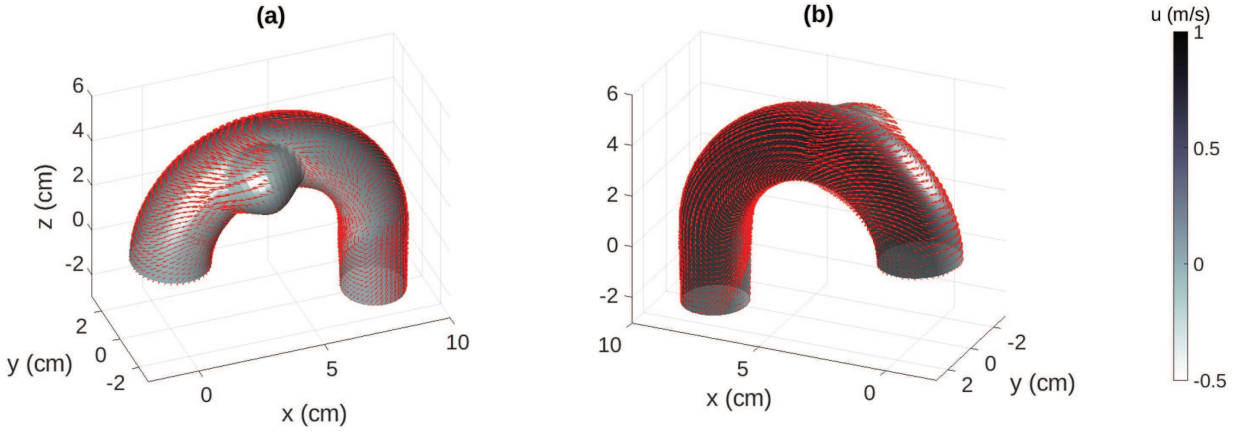

FIGURE 9. Circulation pattern in an idealized aorta vessel with a bulge. Three-dimensional views of the artery with the velocity field at $t = 0.4$ s are shown where the parameters G_o and R_o are given by equations (53) and (54). Panels (a) and (b) show two different views of the vessel. The arrows indicate the 3D velocity field given by equation (49).

velocity contours. Panel (a) shows a section of the artery near the perturbation. The bulge induces a vortex-like structure at time $t = 0.4$ s in the lower region of the bulge but the flow moves in the downstream direction after it passes that region where the artery is less rigid, that is shown at panel (b). The circulation pattern has been extended to a larger region, where the axial velocity is negative in the right side of the artery ($\pi/2 \leq \theta \leq 3\pi/2$) near the bulge and positive on the opposite side. Circulation patterns can be found on other simulations. See for instance [36].

5.5. A discussion about parameter regimes and the numerical results

The numerical tests presented above focused on evaluating different aspects of the model and the scheme. Regarding the model, the main purpose is to show the higher level of details that it can provide when angular variations are allowed in a non-uniform general cross section. One-dimensional models with axi-symmetry have shown to be in good agreement with 3D models and with experimental data, as explained for instance in [18]. The 2D model derived in this work reduces to the 1D counterpart when the vessel's cross sections are axi-symmetric. Even in that case, they can be in good agreement with experimental data. The interested reader can see more details about such comparisons in [18]. Despite the fact that in our setting we are only focusing in idealized aorta simulations, the profiles for the pressure as a function of time is similar to the profiles obtained in this work. The additional attributes in this model that accounts for variations in the angular directions were obtained by assuming very reasonable assumptions. It allows us to obtain more detailed features of the vessel when the cross sections are irregular. It can provide useful information in situations where experimental data could not be available.

Finding detailed experimental data is not an easy task. When available, one can use such data to estimate the model's parameters. For instance, a relation between stress and strain in a dog's artery is shown in [1]. In this context, the strain $\mathcal{R}$ is the ratio between the midwall radius $R = \dfrac{R_E + R_I}{2}$ and the non-stressed midwall radius R_o, $\mathcal{R} = \dfrac{R}{R_o}$. The outer ($R_E$) and inner ($R_I$) vessel's radii be defined as $R_E = R + \frac{1}{2}h_d$, $R_I = R - \frac{1}{2}h_d$,

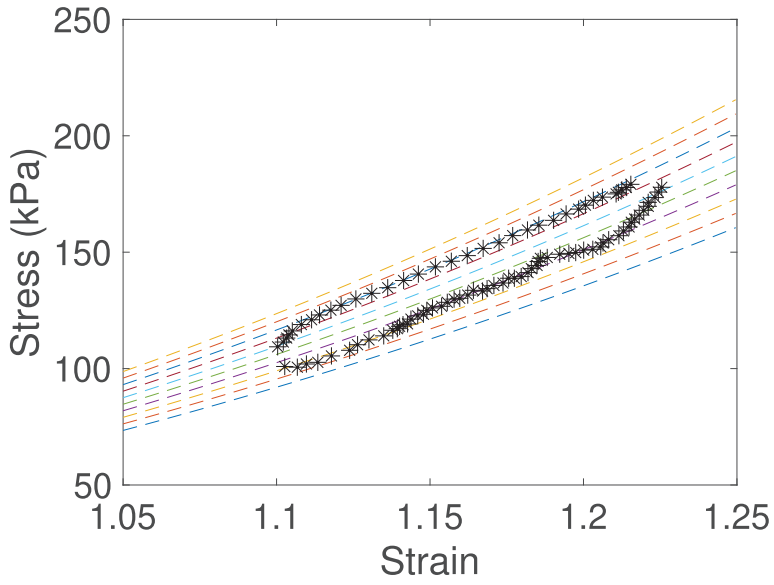

FIGURE 10. Relation between strain and stress in dog's arteries. Experimental data from [1] (bottom panel of Fig. 1) in star symbols and the corresponding curves for different midwall radii R, and fixing the wall thickness $h_d = 0.5$ mm and the $p_o = 9$ kPa. Furthermore, the pressure p was calculated using $\beta = 2$ and G_o is as (29), with $E_Y = 250$ kPa.

where h_d is the wall's thickness. The stress σ is given by

$$\sigma = \frac{2[p_o + p]}{\left(\frac{R}{R_I}\right)^2 - \left(\frac{R}{R_E}\right)^2},$$

where p is transmural pressure (28) and (29). The relation Strain-Stress relates how much an object is deformed respects its initial state and the force that is required to deform it. Figure 10 shows the experimental data in [1] for the strain-stress relation together with different midwall radii R, and fixing the wall thickness $h_d = 0.5$ mm and the $p_o = 9$ kPa. Furthermore, the pressure p was calculated using $\beta = 2$ and G_o is as (29), with $E_Y = 250$ kPa. As we can see, the model's parameters can satisfactorily approximate experimental data when chosen properly. Of course, the parameter values used in our numerical tests are different because they are meant for idealized aorta simulations in humans.

6. Conclusions

Three-dimensional blood flow models provide detailed information of the fluid's evolution, giving accurate and realistic results. However, they involve a high computational cost and are not always a practical tool. As an alternative, one-dimensional models have been derived in the literature. Those models consist of limiting equations that assume the cross sections to be circular with a small radius when compared to the artery's length. Of course, those models involve a low computational cost but they are limited by the conditions used to derive them. Although they have shown to be useful to simulate pressure waves, one looses detailed information of the artery's evolution.

In this work, we have presented a new intermediate two-dimensional model that allows for arbitrary cross sections. The limiting model is valid for small cross-sectional ratios and other reasonable assumptions. We present this model as an alternative with a better balance between realism and computational cost. The resulting system

is conditionally hyperbolic and the spectral properties are described. We have also provided a well-balanced positivity-resulting central-upwind scheme to obtain numerical results. We tested it in idealized aorta models with damaged areas among other scenarios.

In [30], a different expression for the transmural pressure given in (28) is offered in order to consider blood flows in veins. It is also possible to do it in this context as long as the fluid is Newtonian. Furthermore, in such situations one could also consider veins with twists. In the present model, the axis passing through the center of the vessel is assumed to be aligned in the (x, z) plane for simplicity. However, it can be easily generalized to any curve as along as the radius curvature does not exceed the vessel radius. The above research directions will be considered in a future work.

Appendix A. Derivation of the model

The model is derived in this appendix. The first step is the description of the Navier-Stokes equations in cylindrical coordinates, taking into account Fluid-Structure interactions in a moving domain and an elastic membrane. For that end, let us define the gradients in cartesian and cylindrical coordinates by

$$\nabla = (\partial_x, \partial_y, \partial_z), \quad \text{and} \quad \nabla_c = (\partial_s, \partial_r, \partial_\theta), \tag{A.1}$$

respectively, where (x, y, z) and (s, r, θ) are related by equation (1). The corresponding velocity fields are given by

$$\mathbf{V} = (V_x, V_y, V_z), \quad \mathbf{V}_c = (V_s, V_r, V_\theta). \tag{A.2}$$

Applying change of variables, we find that the velocity field in the cylindrical coordinates is given by

$$\begin{aligned} V_s &= \frac{r}{|J|}\{\cos(\alpha(s))V_x + \sin(\alpha(s))V_z\}, \\ V_r &= -\sin(\alpha(s))\sin(\theta)V_x + \cos(\theta)V_y + \cos(\alpha(s))\sin(\theta)V_z, \\ V_\theta &= \frac{1}{r}\{-\sin(\alpha(s))\cos(\theta)V_x - \sin(\theta)V_y + \cos(\alpha(s))\cos(\theta)V_z\}. \end{aligned} \tag{A.3}$$

The partial derivatives in cylindrical coordinates are given in terms of the derivatives in cartesian coordinates by

$$\begin{aligned} \partial_s &= \frac{|J|}{r}\{\cos(\alpha(s))\partial_x + \sin(\alpha(s))\partial_z\} \\ \partial_r &= -\sin(\alpha(s))\sin(\theta)\partial_x + \cos(\theta)\partial_y + \cos(\alpha(s))\sin(\theta)\partial_z \\ \partial_\theta &= r\{-\sin(\alpha(s))\cos(\theta)\partial_x - \sin(\theta)\partial_y + \cos(\alpha(s))\cos(\theta)\partial_z\}. \end{aligned} \tag{A.4}$$

We take the incompressible Navier-Stokes equations with varying density as the full system to be reduced. Such system can be written as

$$\begin{aligned} \frac{D}{Dt}\,\rho &= 0, \\ \frac{D}{Dt}(\rho V_x) &= -\partial_x\, P + \nu\Delta\, V_x, \\ \frac{D}{Dt}(\rho V_y) &= -\partial_y\, P + \nu\Delta\, V_y, \\ \frac{D}{Dt}(\rho V_z) &= -\partial_z\, P + \nu\Delta\, V_z - \rho g, \\ \nabla\cdot\mathbf{V} &= 0. \end{aligned} \tag{A.5}$$

We need to re-write the divergence, material derivative, and Laplacian in cylindrical coordinates. Let (F_1, F_2, F_3) a vectorial field. Then,

$$\nabla \cdot (F_1, F_2, F_3) = \frac{1}{|J|}\nabla_c \cdot \Big[|J|\Big(\tilde{F}_1, \tilde{F}_2, \tilde{F}_3\Big)\Big], \tag{A.6}$$

where the vector field $\Big(\tilde{F}_1, \tilde{F}_2, \tilde{F}_3\Big)$ is given by

$$\begin{aligned}
\tilde{F}_1 &= \frac{r}{|J|}\{\cos(\alpha(s))F_1 + \sin(\alpha(s))F_3\},\\
\tilde{F}_2 &= \cos(\theta)F_2 + \sin(\theta)[-\sin(\alpha(s))F_1 + \cos(\alpha(s))F_3],\\
\tilde{F}_3 &= \frac{1}{r}\{-\sin(\theta)F_2 + \cos(\theta)[-\sin(\alpha(s))F_1 + \cos(\alpha(s))F_3]\}.
\end{aligned} \tag{A.7}$$

In cylindrical coordinates, the material derivative can be expressed as

$$\begin{aligned}
\frac{Df}{Dt} &= \partial_t(f) + \mathbf{V}_c \cdot \nabla_c(f)\\
&= \frac{1}{|J|}\Big\{\partial_t(|J|f) + \nabla_c \cdot (|J|f\mathbf{V}_c) - f\nabla_c \cdot (|J|\mathbf{V}_c)\Big\}.
\end{aligned} \tag{A.8}$$

In the case of incompressible fluids, the last term vanishes and we obtain

$$\frac{Df}{Dt} = \frac{1}{|J|}\{\partial_t(|J|f) + \partial_s(|J|fV_s) + \partial_r(|J|fV_r) + \partial_\theta(|J|fV_\theta)\}. \tag{A.9}$$

Furthermore, the Laplacian can be expressed as

$$\Delta(f) = \frac{1}{|J|}\partial_s\left(\frac{r^2}{|J|}\partial_s\, f\right) + \frac{1}{|J|}\partial_r(|J|\partial_r\, f) + \frac{1}{|J|}\partial_\theta\left(\frac{|J|}{r^2}\partial_\theta\, f\right).$$

Straightforward but long calculations gives the Navier-Stokes equations (1) in cylindrical variables. The new system is given by

$$\begin{aligned}
\frac{D}{Dt}(\rho) &= 0,\\
\frac{D}{Dt}\left(\rho\left[\frac{|J|}{r}\right]^2 V_s\right) &= -\partial_s P_2 + \frac{|J|}{r}\partial_s\left(\frac{|J|}{r}\right)\rho V_s^2 - \sin(\alpha(s))\rho g,\\
&\quad + \nu\Bigg\{\Delta\left(\left[\frac{|J|}{r}\right]^2 V_s\right) - \Delta\left(\left[\frac{|J|}{r}\right]^2\right)V_s + 2\frac{r}{|J|}\partial_r\left[\frac{|J|}{r}\right]\partial_s(V_r)\\
&\quad + 2\frac{r}{|J|}\partial_\theta\left(\frac{|J|}{r}\right)\partial_s(V_\theta) + \nabla_c\left(\frac{r}{|J|}\partial_s\left(\frac{|J|}{r}\right)\right)\cdot\mathbf{V}_c\Bigg\},\\
\frac{D}{Dt}(\rho V_r) &= -\partial_r(P_2) + \frac{|J|}{r}\partial_r\left(\frac{|J|}{r}\right)\rho V_s^2 + r\rho V_\theta^2\\
&\quad + \nu\Bigg\{\Delta(V_r) - 2\frac{r}{|J|}\partial_r\left(\frac{|J|}{r}\right)\partial_s(V_s) - \frac{2}{r}\partial_\theta(V_\theta)\\
&\quad - \left(\frac{r}{|J|}\right)^2\partial_s\left(\frac{|J|}{r}\partial_r\left(\frac{|J|}{r}\right)\right)V_s\\
&\quad - \frac{1}{|J|^2}\left[\left(\frac{|J|}{r}\right)^2 + \left(\frac{|J|}{r} - 1\right)^2\right]V_r - \frac{\partial_r(|J|)\partial_\theta(|J|)}{|J|^2}V_\theta\Bigg\},
\end{aligned} \tag{A.10}$$

$$\begin{aligned}\frac{D}{Dt}\left(\rho r^2 V_\theta\right) &= -\partial_\theta(P_2) + \frac{|J|}{r}\partial_\theta\left(\frac{|J|}{r}\right)\rho V_s^2 \\ &\quad + \nu\Bigg\{\Delta\left(r^2 V_\theta\right) - 2\frac{r}{|J|}\partial_\theta\left(\frac{|J|}{r}\right)\partial_s(V_s) \\ &\quad + \frac{2}{r}\partial_\theta(V_r) - \frac{2}{|J|}\partial_r(|J|rV_\theta) - \left[\frac{r}{|J|}\right]^2\partial_s\left(\frac{|J|}{r}\partial_\theta\left(\frac{|J|}{r}\right)\right)V_s \\ &\quad + \frac{r}{|J|^2}\partial_\theta\left(\frac{|J|}{r}\right)V_r - \left[\frac{r}{|J|}\partial_\theta\left(\frac{|J|}{r}\right)\right]^2 V_\theta\Bigg\}, \\ \nabla_c\cdot(|J|\mathbf{V}_c) &= 0,\end{aligned}$$

where $P_2 = P + r\cos(\alpha(s))\sin(\theta)\rho g$ is the transmural pressure.

A.1. The reduced equations

We carry out an asymptotic analysis to remove small terms in the equations that do not add a significant contribution in the budget and allows us to simplify the model. Following [6], we define $V_{s,0}$, $V_{r,0}$, and $V_{\theta,0}$ be the characteristic radial, axial and angular velocities. Let also λ and R_0 be the characteristic axial and radial lengthscales. Each quantity is non-dimensionalized as $r = R_0\tilde{r}$, $s = \lambda\tilde{s}$, $t = \frac{\lambda}{V_0}\tilde{t}$, $V_s = V_{s,0}\tilde{V}_s$, $V_r = V_{r,0}\tilde{V}_r$, $V_\theta = V_{\theta,0}\tilde{V}_\theta$, $P = \rho V_0^2\tilde{P}$. Following equation (2), the small parameter in this expansion is the ratio between radial and axial lengthscales

$$\epsilon := \frac{R_0}{\lambda} = \frac{V_{r,0}}{V_{s,0}}.$$

This is a reasonable assumption because this ratio is about $\frac{R_0}{\lambda} = \mathcal{O}(10^{-2})$ for the aorta between the renal and iliac arteries

The non-dimensional version of the model is given by

$$\begin{aligned}\frac{\tilde{D}}{Dt}(\tilde{\rho}) &= 0 \\ \frac{\tilde{D}}{Dt}\left(\tilde{\rho}\left[\frac{|\tilde{J}|}{\tilde{r}}\right]^2\tilde{V}_s\right) &= -\frac{[P]}{\rho_0 V_{s,0}^2}\tilde{\partial}_s\,\tilde{P}_2 - \frac{gT}{V_{s,0}}\sin(\alpha(s))\tilde{\rho} + \frac{|\tilde{J}|}{\tilde{r}}\tilde{\partial}_s\left(\frac{|\tilde{J}|}{\tilde{r}}\right)\tilde{\rho}\tilde{V}_s{}^2 \\ &\quad + \frac{\nu T}{\rho_0 R_0^2}\Bigg\{\left(\frac{R_0}{\lambda}\right)^2\frac{1}{|\tilde{J}|}\tilde{\partial}_s\left(\frac{\tilde{r}^2}{|\tilde{J}|}\tilde{\partial}_s\left(\left[\frac{|\tilde{J}|}{\tilde{r}}\right]^2\tilde{V}_s\right)\right) \\ &\quad + \frac{1}{|\tilde{J}|}\tilde{\partial}_r\left(|\tilde{J}|\tilde{\partial}_r\left(\left[\frac{|\tilde{J}|}{\tilde{r}}\right]^2\tilde{V}_s\right)\right) + \frac{1}{|\tilde{J}|}\tilde{\partial}_\theta\left(\frac{|\tilde{J}|}{\tilde{r}^2}\tilde{\partial}_\theta\left(\left[\frac{|\tilde{J}|}{\tilde{r}}\right]^2\tilde{V}_s\right)\right) \\ &\quad + 2\frac{\tilde{r}}{|\tilde{J}|}\tilde{\partial}_r\left(\frac{|\tilde{J}|}{\tilde{r}}\right)\tilde{\partial}_s\left(\tilde{V}_r\right) + 2\frac{\tilde{r}}{|\tilde{J}|}\tilde{\partial}_\theta\left(\frac{|\tilde{J}|}{\tilde{r}}\right)\tilde{\partial}_s\left(\tilde{V}_\theta\right) \\ &\quad + \left(\frac{R_0}{\lambda}\right)^2\tilde{\nabla}_c\left(\frac{\tilde{r}}{|\tilde{J}|}\tilde{\partial}_s\left(\frac{|\tilde{J}|}{\tilde{r}}\right)\right)\cdot\tilde{\mathbf{V}}_c \\ &\quad - \left(\frac{R_0}{\lambda}\right)^2\frac{1}{|\tilde{J}|}\tilde{\partial}_s\left(\frac{\tilde{r}^2}{|\tilde{J}|}\tilde{\partial}_s\left(\left[\frac{|\tilde{J}|}{\tilde{r}}\right]^2\right)\right)\tilde{V}_s\end{aligned}$$

$$
\begin{aligned}
&- \frac{1}{|\tilde{J}|}\tilde{\partial}_r\left(|\tilde{J}|\tilde{\partial}_r\left(\left[\frac{|\tilde{J}|}{\tilde{r}}\right]^2\right)\right)\tilde{V}_s - \frac{1}{|\tilde{J}|}\tilde{\partial}_\theta\left(\frac{|\tilde{J}|}{\tilde{r}^2}\tilde{\partial}_\theta\left(\left[\frac{|\tilde{J}|}{\tilde{r}}\right]^2\right)\right)\tilde{V}_s\Bigg\}\\
\frac{\tilde{D}}{Dt}\left(\tilde{\rho}\tilde{V}_r\right) &= -\frac{[P]}{\rho_0 V_{r,0}^2}\tilde{\partial}_r\,\tilde{P}_2 + \left(\frac{V_{s,0}}{V_{r,0}}\right)^2\frac{|\tilde{J}|}{\tilde{r}}\tilde{\partial}_r\left(\frac{|\tilde{J}|}{\tilde{r}}\right)\tilde{\rho}{\tilde{V}_s}^2 + \tilde{\rho}\tilde{r}{\tilde{V}_\theta}^2\\
&+ \frac{\nu T}{\rho_0 R_0^2}\Bigg\{\left(\frac{R_0}{\lambda}\right)^2\frac{1}{|\tilde{J}|}\tilde{\partial}_s\left(\frac{\tilde{r}^2}{|\tilde{J}|}\tilde{\partial}_s\left(\tilde{V}_r\right)\right) + \frac{1}{|\tilde{J}|}\tilde{\partial}_r\left(|\tilde{J}|\tilde{\partial}_r\left(\tilde{V}_r\right)\right)\\
&+ \frac{1}{|\tilde{J}|}\tilde{\partial}_\theta\left(\frac{|\tilde{J}|}{\tilde{r}^2}\tilde{\partial}_\theta\left(\tilde{V}_r\right)\right) - 2\frac{\tilde{r}}{|\tilde{J}|}\tilde{\partial}_r\left(\frac{|\tilde{J}|}{\tilde{r}}\right)\tilde{\partial}_s\left(\tilde{V}_s\right) - \frac{2}{\tilde{r}}\tilde{\partial}_\theta\left(\tilde{V}_\theta\right)\\
&- \left(\frac{\tilde{r}}{|\tilde{J}|}\right)^2\tilde{\partial}_r\left(\frac{|\tilde{J}|}{\tilde{r}}\right)\tilde{\nabla}_c\left(\frac{|\tilde{J}|}{\tilde{r}}\right)\cdot\tilde{\mathbf{V}}_c\\
&- \frac{\tilde{r}}{|\tilde{J}|}\tilde{\partial}_s\tilde{\partial}_r\left(\frac{|\tilde{J}|}{\tilde{r}}\right)\tilde{V}_s - \frac{1}{\tilde{r}^2}\tilde{V}_r - \frac{1}{|\tilde{J}|}\tilde{\partial}_\theta\left(\frac{|\tilde{J}|}{\tilde{r}}\right)\tilde{V}_\theta\Bigg\}\\
\frac{\tilde{D}}{Dt}\left(\tilde{\rho}(\tilde{r})^2\tilde{V}_\theta\right) &= -\frac{[P]}{\rho_0 R_0^2 V_{\theta,0}^2}\tilde{\partial}_\theta\,\tilde{P}_2 + \left(\frac{V_{s,0}}{R_0 V_{\theta,0}}\right)^2\frac{|\tilde{J}|}{\tilde{r}}\tilde{\partial}_\theta\left(\frac{|\tilde{J}|}{\tilde{r}}\right)\tilde{\rho}{\tilde{V}_s}^2\\
&+ \frac{\nu T}{\rho_0 R_0^2}\Bigg\{\left(\frac{R_0}{\lambda}\right)^2\frac{1}{|\tilde{J}|}\tilde{\partial}_s\left(\frac{\tilde{r}^2}{|\tilde{J}|}\tilde{\partial}_s\left((\tilde{r})^2\tilde{V}_\theta\right)\right) + \frac{1}{|\tilde{J}|}\tilde{\partial}_r\left(|\tilde{J}|\tilde{\partial}_r\left((\tilde{r})^2\tilde{V}_\theta\right)\right)\\
&+ \frac{1}{|\tilde{J}|}\tilde{\partial}_\theta\left(\frac{|\tilde{J}|}{\tilde{r}^2}\tilde{\partial}_\theta\left((\tilde{r})^2\tilde{V}_\theta\right)\right) - \frac{2\tilde{r}}{|\tilde{J}|}\tilde{\partial}_\theta\left(\frac{|\tilde{J}|}{\tilde{r}}\right)\tilde{\partial}_s\left(\tilde{V}_s\right) + \frac{2}{\tilde{r}}\tilde{\partial}_\theta\left(\tilde{V}_r\right)\\
&- \frac{2}{|\tilde{J}|}\tilde{\partial}_r\left(|\tilde{J}|\tilde{r}\tilde{V}_\theta\right) - \left[\frac{\tilde{r}}{|\tilde{J}|}\right]^2\tilde{\partial}_s\left(\frac{|\tilde{J}|}{\tilde{r}}\tilde{\partial}_\theta\left(\frac{|\tilde{J}|}{\tilde{r}}\right)\right)\tilde{V}_s\\
&- \frac{\tilde{r}}{|\tilde{J}|^2}\tilde{\partial}_\theta\left(\frac{|\tilde{J}|}{\tilde{r}}\right)\tilde{V}_r - \left[\frac{\tilde{r}}{|\tilde{J}|}\tilde{\partial}_\theta\left(\frac{|\tilde{J}|}{\tilde{r}}\right)\right]^2\tilde{V}_\theta\Bigg\}\\
\tilde{\nabla}_c\cdot\left(|\tilde{J}|\tilde{\mathbf{V}}_c\right) &= 0.
\end{aligned}
\tag{A.11}
$$

We recall the assumptions (3) and (4), given by

$$
\frac{[P]}{\rho_o V_{s,o}^2} = O(1),\quad \frac{V_{s,o}}{R_o V_{\theta,o}} = O(1),\quad \text{and}\quad \frac{gT}{V_{s,o}} = O(1), R_o|\alpha'(s)| = O(\epsilon),
$$

and

$$
\frac{\nu T}{\rho_o R_o^2} = O(\epsilon).
$$

There is just one leading order term in the momentum equation in the radial direction that is found as follows. The first term in the right-hand side has a factor of

$$
\frac{[P]}{\rho_o V_{r,o}^2} = \frac{[P]}{\rho_o V_{s,o}^2}\frac{V_{s,o}^2}{V_{r,o}^2} = O(\epsilon^{-2}).
$$

The second term has a factor of order $O(\epsilon^{-2})$. However, we ignore that term because

$$
\partial_r(|J|/r) = -\sin(\theta)\alpha'(s)R_o = O(\epsilon).
$$

The viscosity terms are all order $O(\epsilon)$ or higher, and the left-hand side is $O(1)$. Thus, taking the leading order term, we obtain

$$\partial_{\tilde{r}}\left(\tilde{P}_2\right) = 0,$$

which implies that $\tilde{P}_2$ is independent of $\tilde{r}$.

In the equation of balance for the angular momentum, we will exclude only terms that are order $O(\epsilon)$ or higher to keep the contribution of the artery's curvature on the flow. The first term in the right-hand side has a factor

$$\frac{[P]}{\rho_o(R_oV_{\theta,o})^2} = \frac{[P]}{\rho_o V_{s,o}^2}\frac{V_{s,o}^2}{(R_oV_{\theta,o})^2} = O(1),$$

and we keep it. As discussed above, the non-dimensional parameter involving the viscosity term is order $O(\epsilon)$. For the terms inside the brackets, we assume that rV_θ, V_r and $|J|/r$ depend all weakly on θ, which is consistent with the fact that the blood flow moves mainly in the axial direction. As a result, only two terms in front of the viscosity coefficient has a leading contribution, as specified below in equation (5).

Similarly, we only exclude terms in the momentum equation that are order $O(\epsilon)$ or higher. All the terms before the viscosity coefficient are order $O(1)$ or $O(\epsilon)$. Only one viscosity term inside the brackets has a leading contribution. The other terms have either a factor of order $O(\epsilon)$, or can be neglected due to the weak dependance on θ.

The reduced system in dimensional form is given in equation (5) in Section 2.2 . In that equation we redefine $p = P_2$ as the transmural pressure to avoid heavy notation. In Section 2.2, those equations are then integrated in the radial direction to derive the desired model (8).

Acknowledgements. C.A. Rosales-Alcantar was supported by Conacyt National Grant 701892. G. Hernández-Dueñas was supported in part by grants UNAM-DGAPA-PAPIIT IN112222 & Conacyt A1-S-17634. Some simulations were performed at the Laboratorio Nacional de Visualización Científica Avanzada at UNAM Campus Juriquilla, and the Authors received technical support from Luis Aguilar, Alejandro De León, and Jair García from that lab. The co-author G. H-D would like to thank the hospitality of NorthWest Research Associates and the support of UNAM-PASPA-DGAPA during his sabbatical visit.

Conflict of interest. The authors declare that they have no conflict of interest.
Data availability. All data generated during this study are included in this article.
Code availability. All algorithm details are included in this article.

References

[1] R.L. Armentano, J.G. Barra, J. Levenson, A. Simon and R.H. Pichel, Arterial wall mechanics in conscious dogs: assessment of viscous, inertial, and elastic moduli to characterize aortic wall behavior. *Circ. Res.* **76** (1995) 468–478.

[2] C.J. Arthurs, R. Khlebnikov, A. Melville, M. Marčan, A. Gomez, D. Dillon-Murphy, F. Cuomo, M. Silva Vieira, J. Schollenberger, S.R. Lynch *et al.*, Crimson: an open-source software framework for cardiovascular integrated modelling and simulation. *PLOS Comput. Biol.* **17** (2021) 1008881.

[3] N. Bessonov, A. Sequeira, S. Simakov, Y. Vassilevskii and V. Volpert, Methods of blood flow modelling. *Math. Model. Nat. Phenom.* **11** (2016) 1–25.

[4] B.S. Brook, S.A.E.G. Falle and T.J. Pedley, Numerical solutions for unsteady gravity-driven flows in collapsible tubes: evolution and roll-wave instability of a steady state. *J. Fluid Mech.* **396** (1999) 223–256.

[5] S. Čanić, Blood flow through compliant vessels after endovascular repair: wall deformations induced by the discontinuous wall properties. *Comput. Vis. Sci.* **4** (2002) 147–155.

[6] S. Čanić and E.H. Kim, Mathematical analysis of the quasilinear effects in a hyperbolic model blood flow through compliant axi-symmetric vessels. *Math. Methods Appl. Sci.* **26** (2003) 1161–1186.

[7] S. Čanić, C.J. Hartley, D. Rosenstrauch, J. Tambača, G. Guidoboni and A. Mikelić, Blood flow in compliant arteries: an effective viscoelastic reduced model, numerics, and experimental validation. *Ann. Biomed. Eng.* **34** (2006) 575–592.

[8] S. Čanić, M. Galovic, M. Ljulj and J. Tambaca, A dimension-reduction based coupled model of mesh-reinforced shells. *SIAM J. Appl. Math.* **77** (2017) 744–769.

[9] V. Casulli, M. Dumbser and E.F. Toro, Semi-implicit numerical modeling of axially symmetric flows in compliant arterial systems. *Int. J. Numer. Methods Biomed. Eng.* **28** (2012) 257–272.

[10] F. Fambri, M. Dumbser and V. Casulli, An efficient semi-implicit method for three-dimensional non-hydrostatic flows in compliant arterial vessels. *Int. J. Numer. Methods Biomed. Eng.* **30** (2014) 1170–1198.

[11] L. Formaggia, F. Nobile, A. Quarteroni, A. Veneziani and P. Zunino, Advances on numerical modelling of blood flow problems, in European Congress on Computational Methods in Applied Sciences and Engineering (ECCOMAS 2000) (2000) 11–14.

[12] L. Formaggia, D. Lamponi and A. Quarteroni, One-dimensional models for blood flow in arteries. *J. Eng. Math.* **47** (2003) 251–276.

[13] A.J. Geers, I. Larrabide, H.G. Morales and A.F. Frangi, Comparison of steady-state and transient blood flow simulations of intracranial aneurysms, in 2010 Annual International Conference of the IEEE Engineering in Medicine and Biology, IEEE (2010) 2622–2625.

[14] J.-F. Gerbeau, M. Vidrascu and P. Frey, Fluid–structure interaction in blood flows on geometries based on medical imaging. *Comput. Struct.* **83** (2005) 155–165.

[15] S. Gottlieb, C.-W. Shu, and E. Tadmor, Strong stability-preserving high-order time discretization methods. *SIAM Rev.* **43** (2001) 89–112.

[16] G. Guidoboni, R. Glowinski, N. Cavallini and S. Canic, Stable loosely-coupled-type algorithm for fluid–structure interaction in blood flow. *J. Comput. Phys.* **228** (2009) 6916–6937.

[17] D. Ho, A. Squelch and Z. Sun, Modelling of aortic aneurysm and aortic dissection through 3D printing. *J. Med. Radiat. Sci.* **64** (2017) 10–17.

[18] W. Huberts, K. Van Canneyt, P. Segers, S. Eloot, J.H.M. Tordoir, P. Verdonck, F.N. van De Vosse and E.M.H. Bosboom, Experimental validation of a pulse wave propagation model for predicting hemodynamics after vascular access surgery. *J. Biomech.* **45** (2012) 1684–1691.

[19] S. Jerez and M. Uh, A flux-limiter method for modeling blood flow in the aorta artery. *Math. Comput. Modell.* **52** (2010) 962–968.

[20] J. Jung, R.W. Lyczkowski, C.B. Panchal and A. Hassanein, Multiphase hemodynamic simulation of pulsatile flow in a coronary artery. *J. Biomech.* **39** (2006) 2064–2073.

[21] D.N. Ku, Blood flow in arteries. *Ann. Rev. Fluid Mech.* **29** (1997) 399–434.

[22] D.N. Ku, D.P. Giddens, C.K. Zarins and S. Glagov, Pulsatile flow and atherosclerosis in the human carotid bifurcation. Positive correlation between plaque location and low oscillating shear stress. *Arterioscler. Thromb. Vasc. Biol.* **5** (1985) 293–302.

[23] A. Kurganov and G. Petrova, A second-order well-balanced positivity preserving central-upwind scheme for the saint-venant system. *Commun. Math. Sci.* **5** (2007) 133–160.

[24] A. Kurganov and G. Petrova, Central-upwind schemes for two-layer shallow water equations. *SIAM J. Sci. Comput.* **31** (2009) 1742–1773.

[25] A. Kurganov, S. Noelle and G. Petrova, Semidiscrete central-upwind schemes for hyperbolic conservation laws and Hamilton–Jacobi equations. *SIAM J. Sci. Comput.* **23** (2001) 707–740.

[26] F. Kyriakou, W. Dempster and D. Nash, Analysing the cross-section of the abdominal aortic aneurysm neck and its effects on stent deployment. *Sci. Reports* **10** (2020) 1–12.

[27] J. Leibinger, M. Dumbser, U. Iben and I. Wayand, A path-conservative osher-type scheme for axially symmetric compressible flows in flexible visco-elastic tubes. *Appl. Numer. Math.* **105** (2016) 47–63.

[28] G.I. Montecinos, L.O. Müller and E.F. Toro, Hyperbolic reformulation of a 1D viscoelastic blood flow model and ADER finite volume schemes. *J. Comput. Phys.* **266** (2014) 101–123.

[29] L.O. Müller and P.J. Blanco, A high order approximation of hyperbolic conservation laws in networks: application to one-dimensional blood flow. *J. Comput. Phys.* **300** (2015) 423–437.

[30] L.O. Müller, C. Parés and E.F. Toro, Well-balanced high-order numerical schemes for one-dimensional blood flow in vessels with varying mechanical properties. *J. Comput. Phys.* **242** (2013) 53–85.

[31] L.O. Müller, G. Leugering and P.J. Blanco, Consistent treatment of viscoelastic effects at junctions in one-dimensional blood flow models. *J. Comput. Phys.* **314** (2016) 167–193.

[32] A. Quarteroni and L. Formaggia, Mathematical modelling and numerical simulation of the cardiovascular system. *Handb. Numer. Anal.* **12** (2004) 3–127.

[33] A. Quarteroni, A. Veneziani and C. Vergara, Geometric multiscale modeling of the cardiovascular system, between theory and practice. *Comput. Methods Appl. Mech. Eng.* **302** (2016) 193–252.

[34] A. Quarteroni, A. Manzoni and C. Vergara, The cardiovascular system: mathematical modelling, numerical algorithms and clinical applications. *Acta Numer.* **26** (2017) 365–590.

[35] N.P. Smith, A.J. Pullan and P.J. Hunter, An anatomically based model of transient coronary blood flow in the heart. *SIAM J. Appl. Math.* **62** (2002) 990–1018.

[36] F.P.P. Tan, A. Borghi, R.H. Mohiaddin, N.B. Wood, S. Thom and X.Y. Xu, Analysis of flow patterns in a patient-specific thoracic aortic aneurysm model. *Comput. Struct.* **87** (2009) 680–690.

[37] C.A. Taylor and C.A. Figueroa, Patient-specific modeling of cardiovascular mechanics. *Ann. Rev. Biomed. Eng.* **11** (2009) 109–134.

[38] F.N. van de Vosse and N. Stergiopulos, Pulse wave propagation in the arterial tree. *Ann. Rev. Fluid Mech.* **43** (2011) 467–499.

[39] M. Willemet and J. Alastruey, Arterial pressure and flow wave analysis using time-domain 1-D hemodynamics. *Ann. Biomed. Eng.* **43** (2015) 190–206.

[40] N. Xiao, J. Alastruey and C. Alberto Figueroa, A systematic comparison between 1-D and 3-D hemodynamics in compliant arterial models. *Int. J. Numer. Methods Biomed. Eng.* **30** (2014) 204–231.